Journal of Computational Acoustics, Vol. 21, No. 4 (2013) 1350019 (37 pages)

DOI: 10.1142/S0218396X13500197

INTERNATIONAL ASSOCIATION
FOR MATHEMATICS AND
COMPUTERS IN SIMULATION

NUMERICAL SIMULATION OF ACOUSTIC STREAMING WITHIN THE COCHLEA

CHRISTIAN GERSTENBERGER* and FRANZ-ERICH WOLTER†

Division of Computer Graphics, Leibniz University of Hannover
D-30167 Hannover, Germany
**cgerstenberger@welfenlab.de*
†*few@welfenlab.de*

Received 26 January 2013
Accepted 1 September 2013
Published 5 December 2013

This paper is concerned with the numerical examination of acoustically driven flows within the inner ear on the basis of a computational model. For this purpose, a comprehensive system of differential equations and boundary conditions is deduced, which takes, to a satisfactory extent, the complexity of the main biophysical mechanisms of the cochlea into account. Beside an appropriate representation of the fluid dynamics, also the biomechanical properties of the basilar membrane as well as the internal amplification mechanism caused by the outer hair cell motility are considered in order to get realistic estimates of the structure and magnitude of the mean flow field. The present paper introduces a two-stage approach for the numerical evaluation of the solutions on the basis of the finite element method. The first step deals with the calculation of the linear acoustic reaction whereas the second step is associated with the determination of a first-order approximation of the acoustic streaming field. It is shown that the results are essentially consistent with measurements as well as analytical and experimental considerations. In addition, the numerical estimates of the acoustically driven flows provide an instrument for a more profound discussion on their physiological impact.

Keywords: Acoustic streaming; cochlea; fluid-structure interaction.

1. Introduction

The term *acoustic streaming* is associated with the mean motions of a fluid or a gas which are induced by an acoustic field. The relevance of acoustically driven flows and its potential influence on the physiological processes of the cochlea are still an open issue. Up to now, a direct examination of such mean flows within the cochlea has not yet been possible due to the limited accessibility and the small dimensions of the liquid filled chambers. Furthermore, it can be expected that the resultant velocities of the acoustic streaming field are relatively small in comparison to the characteristic velocities of the sound field. This work yields

numerical estimates of the magnitudes as well as the structure of acoustic streaming within the cochlea on the basis of a simulation process. The objective of this computational model is the provision of a new instrument for a substantiated discussion on the physiological impact of acoustically driven flows within the cochlea. In addition, a completely new approach for simulating acoustic streaming within a fluid-structure coupled system like the inner ear is proposed which might also be used in a wide range of other applications.

Two very important contributions to the subject of acoustic streaming within the inner ear, which arise from the cochlear travelling waves, come from Hallauer[1] and Lighthill.[2] Hallauer as well as Lighthill examined the acoustic driven flows on the basis of theoretical considerations. Both approaches use mathematical asymptotic and perturbation techniques in order to get approximations of the nonlinear fluid motion within the cochlea. While Lighthill focusses on the determination of an estimate of the potential velocities of acoustic streaming, Hallauer also calculates the streamlines of the acoustically driven motions on the basis of his mathematical model.

In contrast to the theoretical considerations from Lighthill and Hallauer, an experimental examination of acoustic streaming can be traced back to Békésy.[3] In his pioneering work he performed inter alia studies on mechanical cochlear models. He observed that above and below the cochlear partition two eddies arise if the mechanical model is stimulated by a sinusoidal excitation. It turns out that this eddy-like motion can be associated with the term acoustic streaming. A detailed description of these eddy-like mean flows was carried out by Tonndorf.[4]

Acoustic streaming has already been studied in a lot of numerical simulation processes. Different kinds of numerical approaches for the simulation of acoustic streaming were, for example, reviewed by Boluriaan and Morris.[5] But up to now, it has not yet succeeded to establish an adequate method for the numerical simulation of acoustic streaming within biophysical systems like the cochlea. The primary reason for this lies in the fact that the velocity field of the fluid is mainly influenced by the interactions with its adjacent structures.

In this work, a well-proven numerical method is adapted that was successfully implemented by Köster,[6] who studied the structure of acoustic streaming caused by piezoelectrically driven microfluidic bio-chips. Köster used a standard perturbation technique in order to split the nonlinear acoustic streaming problem into two linear subproblems. His computational model also includes a more precise treatment of the acoustic radiator, as originally suggested by Bradley.[7]

To investigate the influence of acoustically driven flows in the inner ear, an appropriate computational model was developed, which has been studied in a simulation process. In contrast to the work from Köster,[6] this computational model consists not only of a fluid-domain but also of structural components that have a significant influence on the fluid. A schematic layout of the model is shown in Fig. 1. As one can see, the model introduced in this paper can also be divided into a first-order system and a second-order system. The first-order system describes the linear acoustics within the fluid-domain in combination with the mutual interactions of the cochlear structures, such as the basilar membrane, the oval window and the round window. The oval window serves as an acoustic radiator

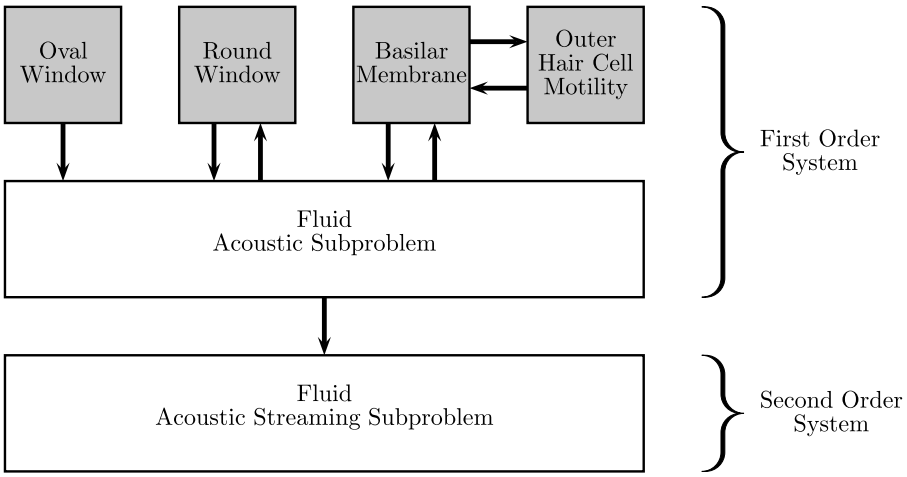

Fig. 1. Schematic layout of the computational model used for simulation of acoustically driven flows within the cochlea. On the basis of a perturbation technique, the system is separated into first- and a second-order system. The first-order system describes the linear acoustic field of the fluid as well as its interactions with the structures, such as the oval window, the round window and the basilar membrane. Furthermore, the motility of the outer hair cells is taken into account which results in additional forces acting on the basilar membrane. The first-order system provides results that can be used by the second-order system in order to calculate an approximation of acoustic streaming.

due to the direct contact with the stapes of the middle ear. The round window is covered by a membrane that allows the fluid to move arbitrarily to a certain degree. The basilar membrane can also be brought into motion due to the difference of the pressure above and below the cochlear partition. In turn, such a displacement of the basilar membrane also has an influence on the velocity field of its adjacent fluid. Furthermore, an additional force term that acts on the basilar membrane has also to be taken into account for the first-order subproblem in order to represent the motility of the outer hair cells. At a second stage the acoustically driven flows can be determined on the basis of the results of this first-order system.

2. Modeling

In order to obtain an implementable model of the cochlea some simplifications and assumptions are made while maintaining fundamental aspects to get a valid representation for estimating the occurrence and structure of acoustically driven flows within the fluid-filled chambers of the inner ear. The most substantial simplification of the model presented here is that the dynamics of the cochlea are simulated on the basis of a simplified two-dimensional domain as illustrated in Fig. 2. Three-dimensional models of the cochlea were, for instance, realized by Givelberg and Bunn[8] who used the *immersed boundary method*, as well as by Cheng *et al.*[9] and Böhnke and Arnold[10] who performed *finite element simulations*. In contrast to these computationally intensive approaches, Lim and Steele[11] introduced a significantly faster three-dimensional model that is based on the WKB-method and which takes

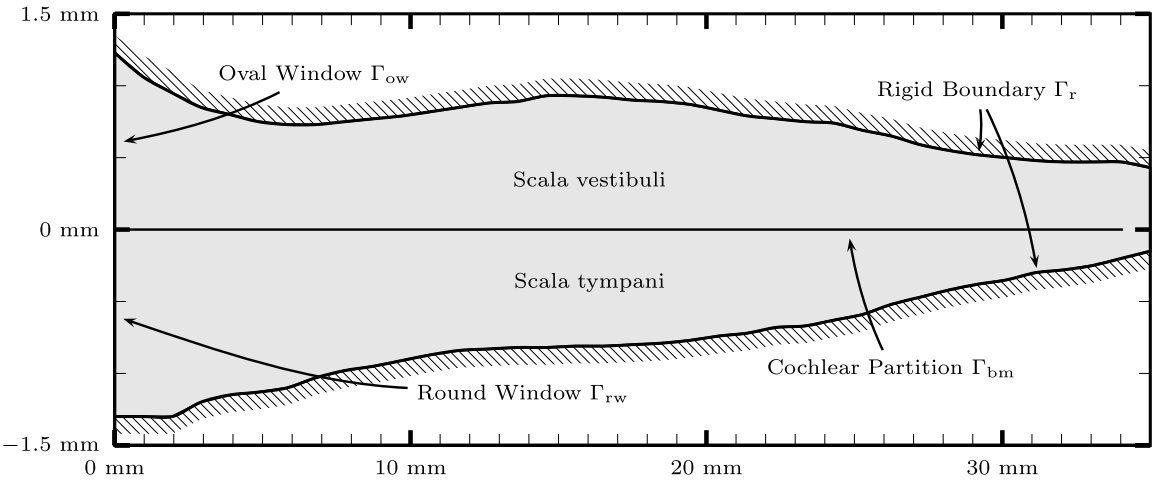

Fig. 2. The two-dimensional shape of the uncoiled human cochlea model. The heights of the scala vestibuli and scala tympani are taken from Wysocki.[13] The scala vestibuli and the scala tympani constitute the fluid domain Ω and these chambers are bordered by the rigid boundary Γ_r, the oval window Γ_{ow} and the round window Γ_{rw}. Both ducts are separated by the cochlear partition Γ_{bm} which serves as a simplified representation of the *basilar membrane* in combination with the *organ of corti*. For reasons of simplicity the scala media is not explicitly taken into account by the model. The oval window consists of the *stapes* which act as an acoustic radiator in order to stimulate the cochlear system. The piston-like motions of the stapes can be represented by corresponding displacements of the associated boundary. In contrast, the round window is closed by a flexible membrane which allows, to a certain extent, a free motion of the fluid.

the nonlinear behavior as well as the feed forward mechanism of the basilar membrane into account. This approach was developed further by Yoon *et al.*[12] in order to achieve a better correlation with *in vivo* measurements. However, the occurrence of acoustically driven flows could not be investigated by these models, due to simplifying assumptions made by the modeling process. Even though the results presented here are based on a two-dimensional domain, this work provides a basic concept for analyzing acoustic streaming also in a three-dimensional reference system.

2.1. *Fluid dynamics*

2.1.1. *Conservation equations*

The dynamics of the perilymph are described on the basis of different conservation principles. The *conservation of mass* can be written as

$$\frac{\partial \rho}{\partial t} = -\mathrm{div}(\rho \boldsymbol{v}), \tag{1}$$

where $\rho(\boldsymbol{x}, t)$ denotes the scalar density field, $\boldsymbol{v}(\boldsymbol{x}, t)$ the vectorial velocity field and t the time-parameter. The spatial coordinates $\boldsymbol{x} = (x, y)$ consist of the longitudinal component x and the vertical component y. The *conservation of linear momentum* can be expressed in

terms of the *stress tensor* $\boldsymbol{\sigma}$ as

$$\rho\left(\frac{\partial \boldsymbol{v}}{\partial t} + (\operatorname{grad} \boldsymbol{v}) \cdot \boldsymbol{v}\right) = \operatorname{div} \boldsymbol{\sigma}. \tag{2}$$

It should be noted that both conservation equations are formulated on the basis of the *Eulerian specification* of motion. As a result of the *conservation of angular momentum* the stress tensor $\boldsymbol{\sigma}$ must be symmetric.[14]

2.1.2. *Constitutive relations*

In order to identify a unique solution of these different field functions the system of equations must be supplemented by further relations that are usually referred to as *constitutive relations*. It turned out that the dynamics of a variety of different fluids and gases for a wide range of applications can be modeled very well if a linear relationship between the deviatoric stress and the strain rate is assumed. In conformity with some basic assumptions of material theory, the stress tensor can be expressed as

$$\boldsymbol{\sigma} = -p\boldsymbol{I} + \left(\zeta - \frac{2}{3}\eta\right) \operatorname{tr}(\boldsymbol{D})\boldsymbol{I} + 2\eta\boldsymbol{D}, \tag{3}$$

where $\boldsymbol{D}$ is the tensor that quantifies the strain rate.[15,16,a] The coefficients η and ζ can be associated with the *shear viscosity* and the *bulk viscosity* of the fluid.

In acoustics, the deviations of the pressure and the density from its respective ambient values can be approximated by the linear relationship

$$p - p^{(0)} = \left.\frac{\partial p}{\partial \rho}\right|_{\rho^{(0)}} (\rho - \rho^{(0)}) = {c_0}^2(\rho - \rho^{(0)}), \tag{4}$$

where the constant of proportionality can be identified as the square of the so-called *small signal sound speed* c_0. Since the exact specifications of the perilymph are not known, the properties of the fluid are assumed to be similar to water at room temperature (cf. Table 1).

2.1.3. *Boundary conditions*

At the boundaries it is assumed that the *no-slip condition* can be applied, which means that the velocity of the viscous perilymph is equal to the velocity of the boundaries. At the rigid boundaries, this condition can simply be stated as

$$\boldsymbol{v}(\boldsymbol{x}, t) = \boldsymbol{0} \quad \text{for all } \boldsymbol{x} \in \Gamma_{\mathrm{r}}. \tag{5}$$

[a]In terms of the velocity field $\boldsymbol{v}$, the strain rate can be written as $\boldsymbol{D} = \frac{1}{2}\big(\operatorname{grad} \boldsymbol{v} + (\operatorname{grad} \boldsymbol{v})^T\big)$.[15]

Table 1. Physical constants that are needed for the simulation of the fluid dynamics. The values are based on the physical properties of water at room temperature.

Symbol	Value	Name	Unit
$\rho^{(0)}$	998.0	Ambient density	kg/m^3
c_0	1484.0	Small signal sound speed	m/s
ζ	3.0×10^{-3}	Bulk viscosity	Ns/m^2
η	1.0×10^{-3}	Shear viscosity	Ns/m^2

But in the case of the moving boundaries (oval window and basilar membrane), the no-slip condition can be evaluated to

$$\boldsymbol{v}(\boldsymbol{x}_0 + \boldsymbol{\zeta}(\boldsymbol{x}_0, t), t) = \frac{\partial \boldsymbol{\zeta}(\boldsymbol{x}_0, t)}{\partial t}, \tag{6}$$

where $\boldsymbol{\zeta}(\boldsymbol{x}_0, t)$ describes the displacement of the boundary from its resting position $\boldsymbol{x}_0$.

For the purpose of simplification explicit changes of the domain, caused by the displacements of the moving boundaries, are neglected. This simplification is reasonable and possible, since the oscillations of the boundaries are substantially smaller than the proportions of the cochlea model. Equation (6) constitutes a Lagrangian specification of the velocity at the boundary. For the adaption of the boundary condition to an Eulerian specification, a vectorial Taylor expansion of the left-hand side can be performed to obtain

$$\boldsymbol{v}(\boldsymbol{x}_0, t) = \frac{\partial \boldsymbol{\zeta}}{\partial t} - \Big(\operatorname{grad} \boldsymbol{v}(\boldsymbol{x}_0, t)\Big) \cdot \boldsymbol{\zeta} - \cdots. \tag{7}$$

Furthermore, it is assumed that no external forces act on the fluid across the outer boundaries. In terms of the stress tensor $\boldsymbol{\sigma}$, this condition can be written as

$$\boldsymbol{\sigma}(\boldsymbol{x}, t) \cdot \boldsymbol{n}(\boldsymbol{x}, t) = 0 \quad \text{for all } \boldsymbol{x} \in \Gamma, \tag{8}$$

where $\boldsymbol{n}$ indicates the (unit) outward normal vector with respect to the boundary of the fluid volume. At the beginning of the simulation process t_0, it is presumed that the system is at rest.

2.1.4. *Perturbation expansion*

Since the acoustically driven flows are dominated by viscous forces (and not by inertial forces), the streaming can be characterized by a low *Reynolds number*. In the case of low Reynolds numbers the use of a perturbation technique has advantages over the fully nonlinear approach, since the perturbation approach represents the nonlinear problem by a set of linear subproblems. Normally, it is sufficient to consider only the first two linear subproblems. This perturbation method has already been successfully adopted by several authors.[6,7,17]

For the implementation of the perturbation approach, the unknown functions are represented by perturbation expansions in the small *Mach number* $\epsilon \ll 1$. The Taylor series of the velocity-field is, for instance, given by

$$\boldsymbol{v}(\boldsymbol{x},t,\epsilon) = \underbrace{\boldsymbol{v}(\boldsymbol{x},t,\epsilon)|_{\epsilon=0}}_{=:\boldsymbol{v}^{(0)}} + \underbrace{\left.\frac{\partial \boldsymbol{v}(\boldsymbol{x},t,\epsilon)}{\partial \epsilon}\right|_{\epsilon=0}}_{=:\boldsymbol{v}^{(1)}}\epsilon + \underbrace{\left.\frac{\partial^2 \boldsymbol{v}(\boldsymbol{x},t,\epsilon)}{\partial \epsilon^2}\right|_{\epsilon=0}}_{=:\boldsymbol{v}^{(2)}}\epsilon^2 + \mathcal{O}(\epsilon^3). \tag{9}$$

Similarly, the other field-functions (pressure, density, etc.) can also be represented by such a perturbation expansion in ϵ. This approach is, of course, only applicable under the assumption that the perturbed problem arises smoothly from an initial problem through the continuous variation of the parameter ϵ.

This procedure is based on the principle that terms of different order are independent from each other.[18] This means that, after substituting the respective perturbation expansions for the unknown functions, each equation can be separated into a set of equations, whereby each relation consists only of terms of the same order.

Lighthill[17] pointed out that this separation of different terms should primarily depend on their numerical dimension and not on their mathematical order. He concluded that the resultant second-order system, which is used for the evaluation of acoustic streaming, neglects a fourth-order quantity that would take inertial effects of the mean flows into account. These inertial effects become more and more significant for applications that are characterized by a high Reynolds number. In these cases, the successive perturbation method would probably fail to approximate the mean flows correctly.

In steady state, the first-order functions describe the harmonic excess values of the fundamental acoustic field with the angular frequency ω, provided that the system is stimulated by a sinusoidal excitation of the same frequency. Then, the second-order functions can be associated with the second-order harmonic field of double the frequency as well as a second-order steady streaming.[6,7] In this work, the main focus lies on the determination of this secondary steady flow field, since it constitutes a first-order approximation of acoustic streaming. Any higher-order mean flows are neglected, due to the rapid decrease of their magnitudes.

2.2. *The first-order system*

2.2.1. *The acoustic subproblem*

After substituting the perturbation expansions for the velocity-, pressure- and density-functions and considering only the first-order terms, the acoustic subproblem can be expressed as

$$\frac{1}{{c_0}^2}\frac{\partial p^{(1)}}{\partial t} = -\rho^{(0)}\,\mathrm{div}\,\boldsymbol{v}^{(1)}, \tag{10}$$

$$\rho^{(0)}\frac{\partial \boldsymbol{v}^{(1)}}{\partial t} = -\mathrm{grad}\,p^{(1)} + \left(\zeta + \frac{\eta}{3}\right)\mathrm{grad}\,\mathrm{div}\,\boldsymbol{v}^{(1)} + \eta\,\Delta\,\boldsymbol{v}^{(1)}. \tag{11}$$

According to Eq. (7), the first-order approximation of the Eulerian specification of the no-slip condition can be evaluated by taking only the first-order term into account. Therefore, the first-order velocity components at the basilar membrane and at the oval window can be written in terms of the displacements of the cochlear partition ξ and the oval window ξ_{ow} as

$$\boldsymbol{v}^{(1)}(\boldsymbol{x},t) = \begin{bmatrix} 0 & \dfrac{\partial}{\partial t}\xi(\boldsymbol{x},t) \end{bmatrix}^T \qquad \text{for all } \boldsymbol{x} \in \Gamma_{\text{bm}}, \tag{12}$$

$$\boldsymbol{v}^{(1)}(\boldsymbol{x},t) = \begin{bmatrix} \dfrac{\partial}{\partial t}\xi_{\text{ow}}(\boldsymbol{x},t) & 0 \end{bmatrix}^T \qquad \text{for all } \boldsymbol{x} \in \Gamma_{\text{ow}}. \tag{13}$$

2.2.2. *The passive mechanics of the cochlear partition*

The interactions between the fluid and the basilar membrane have a significant influence on the sound field within the inner ear. Therefore, it is essential to take the mechanical behavior of the cochlear partition into account. In this context, an approach, developed by Mammano and Nobili,[19,20] is adapted that has proven to be a well-functioning one-dimensional model for describing the deflections of the basilar membrane as cause of the pressure differences across the partition.

Their model is based on the idea that the dynamic reaction of the basilar membrane can, in principle, be described by an array of oscillators, which are characterized by different physical properties. Figure 3 shows a schematic illustration of such an array of oscillators. Each oscillator consists of a mass which can be set into vibration through a spring. The springs are characterized by its respective stiffness. Furthermore each spring-mass system is attached to a damper which tends to reduce the oscillation.

But in contrast to such a discrete arrangement of individual oscillators, the basilar membrane is rather modeled as a continuum represented by the one-dimensional cochlear partition as shown in Fig. 2. According to Mammano and Nobili,[19] such a damped oscillation

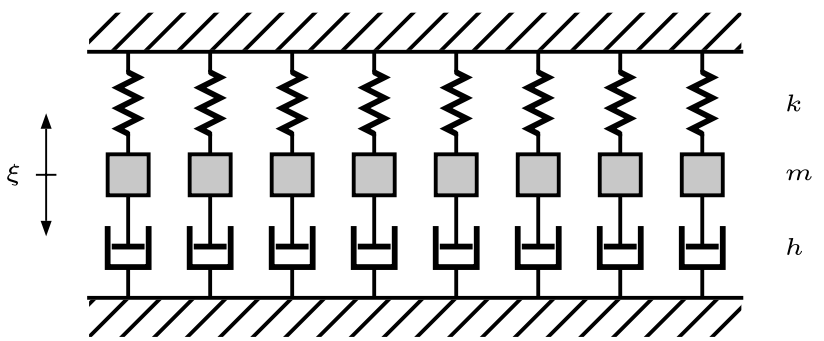

Fig. 3. The mechanical properties of the basilar membrane can be represented by an array of damped oscillators. Each oscillator is characterized by its specific mass m, viscosity h and stiffness k. Vertical displacements $\xi(x)$ are caused by external forces.

of a continuous one-dimensional system that describes the vertical displacement of the basilar membrane $\xi(x,t)$ under the action of external forces $f(x,t)$, can be represented by the differential equation

$$m(x)\frac{\partial^2\xi(x,t)}{\partial t^2} + h(x)\frac{\partial\xi(x,t)}{\partial t} + k(x)\xi(x,t) = f_{p_+}(x,t) - f_{p_-}(x,t) + \vartheta(x,t) \tag{14}$$

if it is assumed that all forces depend linearly on the displacement of the basilar membrane. The coefficient functions describe different physical properties of the basilar membrane. An adequate choice of these parameter functions is not easy, because the structure of the organ of corti is not homogeneous and the material properties are difficult to determine. Furthermore, it is not clear to what extent certain characteristics may be relevant for the oscillation process. However, in order to ensure that the coefficients range within the physical limits, they are estimated on the basis of some theoretical and dimensional considerations having regard to the biophysical structure of the organ of corti (cf. Fig. 4).

The right-hand side of Eq. (14) considers external forces acting on the basilar membrane. As a result of the fluid pressure above and below the basilar membrane, two hydrodynamic forces are acting on the cochlear partition. Since the pressure acts — at a specific location x — on the whole width $w_{\mathrm{bm}}(x)$ of the basilar membrane, the two components of the hydrodynamic force per unit length may be written as

$$f_{p_\pm}(x,t) = \frac{1}{2} w_{\mathrm{bm}}(x)\; p^{(1)}(\boldsymbol{x},t)\big|_{\boldsymbol{x}=(x,\pm 0)}. \tag{15}$$

Due to the assignment of two different pressure values at the location $\boldsymbol{x} = (x,0)$ (caused by the one-dimensional representation of the basilar membrane), the second components of the coordinates are also labeled by a sign to indicate the location. Thus, a positive (negative)

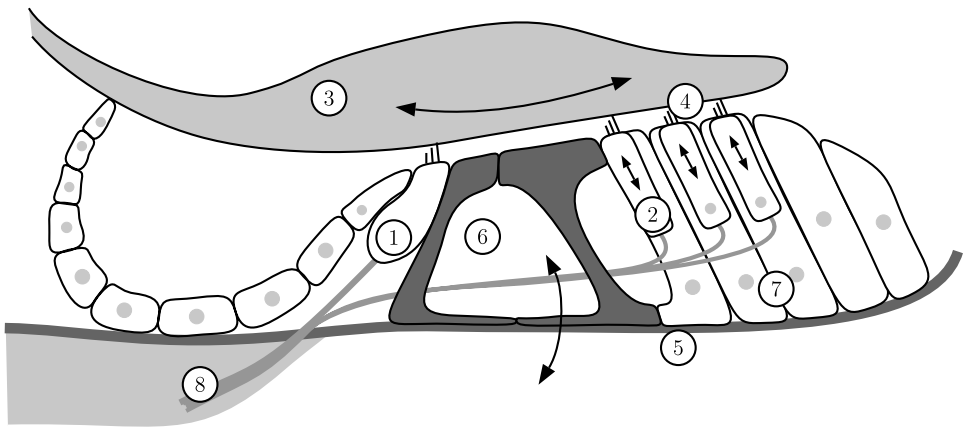

Fig. 4. Cross-section of a mammalian organ of corti: (1) Inner hair cell, (2) outer hair cells, (3) tectorial membrane, (4) stereocilia, (5) basilar membrane, (6) tunnel of corti, (7) cells of deiters and (8) Nerve fibres. The arrows indicate the principal motions of the organ of corti. The pressure difference between the upper and lower chamber causes upward and downward movements of the basilar membrane. Furthermore, the tectorial membrane moves along the reticular laminar due to their different pivots.

sign refers to the location that belongs to the upper (lower) duct. Actually, due to the anatomical structure and the lateral fixation of a basilar membrane segment (cf. Fig. 4), the pressure should not be accumulated uniformly along the radial width. This issue is taken into account (in a simplified manner) by introducing an effective width which is assumed to be half of the geometric width.

The force ϑ is associated to the internal amplification mechanism provided by the outer hair cells.

2.2.3. *Outer hair cell motility*

The vertical motions of the basilar membrane are accompanied with a shearing displacement of the tectorial membrane in relation to the reticular lamina. This kind of motion is the result of different pivots of the tectorial membrane and the reticular lamina around which they rotate.[19] The stereocilia of the outer hair cells are deflected by the shearing flow of the endolymph and due to a partial contact of the stereocilia with the bottom of the tectorial membrane. The deflection of these hair bundles causes in turn a change of the cell potential due to a mechanoelectrical transduction mechanism. If the stereocilia are deflected in the direction of their tallest outgrowth, the outer hair cell will be depolarized. Otherwise, a hyperpolarization is caused by a deflection in the opposite direction. As a result of electrical stimulation the outer hair cells are capable of changing length. Therefore, the length change is often referred to as *electromotility*.

Because this work is not primarily concerned with an exact representation of the complex processes of the outer hair cell motility, a simplified stimulus-response model is adapted as it was suggested by Nobili *et al.*[20] in order to take the feedback from the outer hair cells into account. Therefore, it is assumed that the relationship between the deflection ζ of the hair bundles and the force ϑ can be represented by

$$\vartheta(x, \zeta(x,t)) = \alpha(x)\,\mathrm{sig}(\beta(x)\zeta(x,t)), \tag{16}$$

where sig is a sigmoid function[b] and $\alpha(x)$ and $\beta(x)$ are parameters that depend on the specific internal processes involved in the outer hair cell motility. For small deflections of the hair-bundles these saturation-effects can be neglected and Eq. (16) can be linearly approximated by

$$\vartheta(x, \zeta(x,t)) \approx \alpha(x)\beta(x)\zeta(x,t). \tag{17}$$

Since this approximation neglects the nonlinear saturation effects that limit the outer hair cell driven force, relation (17) only holds true for small deflections of the hair-bundles.

[b]The sigmoid function used in this work is defined as $\mathrm{sig}(x) := 1 - \frac{2}{\mathrm{e}^{2x}+1}$. The sigmoid function is chosen in such a way that its values ranges from -1 to 1 and that its slope at the origin is equal to 1.

The specification of the constant of proportionality $\alpha(x)\beta(x)$ is based on some phenomenological considerations that are targeted on the realization of the outer hair cell driven amplification mechanism.[19–22]

In order to calculate the force-feedback the deflection of the hair-bundles have to be determined on the basis of the vertical displacement of the basilar membrane. It is assumed that the motions of the tectorial membrane relative to the reticular laminar can be represented as a separate oscillator and that this subsystem is mainly stimulated by the vertical acceleration of the basilar membrane displacements. In terms of a linear differential equation and according to Mammano and Nobili[19,20] the deflection ζ of the hair bundles can therefore be written as

$$m_{\mathrm{tm}}(x)\frac{\partial^2\zeta(x,t)}{\partial t^2} + h_{\mathrm{tm}}(x)\frac{\partial\zeta(x,t)}{\partial t} + k_{\mathrm{tm}}(x)\zeta(x,t) = g_{\mathrm{tm}}(x)m_{\mathrm{tm}}(x)\frac{\partial^2\xi(x,t)}{\partial t^2}, \qquad (18)$$

where $m_{\mathrm{tm}}(x)$, $h_{\mathrm{tm}}(x)$ and $k_{\mathrm{tm}}(x)$ are coefficient functions used for constituting the specific inertia, damping and stiffness of the oscillating subsystem. These coefficient functions are specified on the basis of some dimensional and theoretical considerations. Due to the different orientation of the subsystem and due to some internal losses of the coupling, the external force acting on the subsystem is only a fraction of the vertical acceleration driven forces. This effect was taken into account by the additional gain function $g_{\mathrm{tm}}(x)$. According to Nobili *et al.*,[20] it is assumed that the gain function is constant along the cochlear partition and that the effective force acting on the subsystem is only a tenth of the vertical inertial force.

On the basis of these assumptions, it can be shown that the outer hair cell force ϑ acts, in principle, as a negative damping term (cf. Mammano and Nobili[19] and Nobili *et al.*[20]). In order to guarantee the stability of the system, the amount of negative damping caused by the outer hair cells should not exceed the amount of positional damping described by the second term on the left-hand side of Eq. (14). Therefore, it makes sense to use an additional control parameter $\lambda(x)$ (hereinafter referred to as *outer hair cell activity parameter*) that specifies the degree of damping cancellation. If λ is equal to one, the total positional viscosity can potentially be canceled by the outer hair cell driven force. In contrast, no additional outer hair cell force will be applied if λ is equal to zero.

2.3. *The second-order system*

2.3.1. *The acoustic streaming subproblem*

The acoustic streaming subproblem is established on the basis of the second-order system that results from the perturbation approach as described in Sec. 2.1.4. In steady state, the second-order equations are associated with the second harmonic fields in combination with a steady flow field. While the determination of the second harmonic field is of no interest to this work, the evaluation of the steady flow field yields a first-order approximation of acoustic streaming. In order to extract the steady flow field (hereinafter indicated by the superscript

(dc)) from the second-order system, the operator $\langle\cdot\rangle$ that determines the temporal average of time-dependent functions can be applied. The mean of the second-order equation that is associated with the balance-of-mass principle 1 can be written as

$$\rho^{(0)} \operatorname{div} \boldsymbol{v}^{(dc)} = \tilde{m}, \tag{19}$$

where the term $\tilde{m}$ corresponds with a virtual mass-source. This source distribution is caused by the first-order acoustic subproblem and describes the supply of mass.[7] In terms of the first-order fields, the mass-source can be evaluated to

$$\tilde{m} = -\frac{1}{{c_0}^2} \operatorname{div}\langle p^{(1)} \boldsymbol{v}^{(1)}\rangle. \tag{20}$$

Similarly, the steady components of the secondary flow fields must fulfill the time-averaged second-order version of the balance-of-momentum principle 2, which is given by

$$\operatorname{grad} p^{(dc)} - \left(\zeta + \frac{\eta}{3}\right) \operatorname{grad} \operatorname{div} \boldsymbol{v}^{(dc)} - \eta \Delta \boldsymbol{v}^{(dc)} = \tilde{\boldsymbol{f}}, \tag{21}$$

where $\tilde{\boldsymbol{f}}$ denotes a virtual force-source distribution. The force-source acts as an external volume-force and depends on the acoustic field. By using first-order terms, the force-source distribution can be expressed as

$$\tilde{\boldsymbol{f}} = -\frac{1}{{c_0}^2} \left\langle p^{(1)} \frac{\partial \boldsymbol{v}^{(1)}}{\partial t} \right\rangle - \rho^{(0)} \langle (\operatorname{grad} \boldsymbol{v}^{(1)}) \boldsymbol{v}^{(1)} \rangle. \tag{22}$$

By substituting the respective perturbation expansion for the field variables of Eq. (7) and by applying the mean-operator, the time-averaged second-order boundary condition can be written as

$$\boldsymbol{v}^{(dc)} = -\langle (\operatorname{grad} \boldsymbol{v}^{(1)}) \boldsymbol{\zeta}^{(1)} \rangle. \tag{23}$$

A more detailed discussion about this second system with respect to its physical meaning and its connection to acoustic streaming can, for instance, be found in the paper from Bradley.[7]

3. Implementation

3.1. *Meshing*

In the context of this work, the mesh generation is based on specific local refinements of a coarse mesh in order to minimize potential errors between the exact solution and its numerical approximation on the one hand and on the other to limit the computational effort of the simulation process. Therefore, an initial marking-routine is used which specifies for each element the number of refinements that should be performed by the refinement procedure. The typical traveling wave motion of the basilar membrane displacement (as described in detail

in Sec. 4.1.1) is a result of its interactions with the adjacent fluid. According to Olson[23,24] who measured the fluid motion close to the basilar membrane with pressure gradient measurements, the displacement pattern of the basilar membrane is reflected in the fluid to a certain extent. The significant increase of the amplitude of the traveling wave (until the maximum is reached) in combination with a substantial decrease of its wave length indicates that the fluctuations of the field variables increase along the cochlear partition up to the point where the traveling wave dissipates.

Another important aspect (as discussed in detail in Sec. 4.1.2) is that the field variables within the thin *Stokes boundary layer* next to the basilar membrane should be accurately approximated by the finite element space. According to Lighthill,[17] the thickness of this Stokes boundary layer can be estimated to range from about 10 μm to 400 μm in dependence of the stimulation frequency of audible sound.

On the basis of these heuristic arguments, the number of refinements of the elements next to the basilar membrane is gradually increased along the partition until a specific location is reached. This location is specified by the expected decay of the traveling wave, which can be estimated by using the frequency-position map from Greenwood[25] as described in Sec. 4.1.1.

In addition to the fluid domain, also the basilar membrane and its interactions with the fluid have to be taken into account by the numerical implementation. As already described above, the basilar membrane should be represented by a one-dimensional line between the fluid-filled chambers. The additional one-dimensional mesh is constructed in such a way that the individual line segments coincide with the corresponding boundary edges of the fluid domain. This identical arrangement of the meshes with respect to the location and width of each line segment is not mandatory, but it significantly simplifies the numerical realization of the fluid structure interaction.

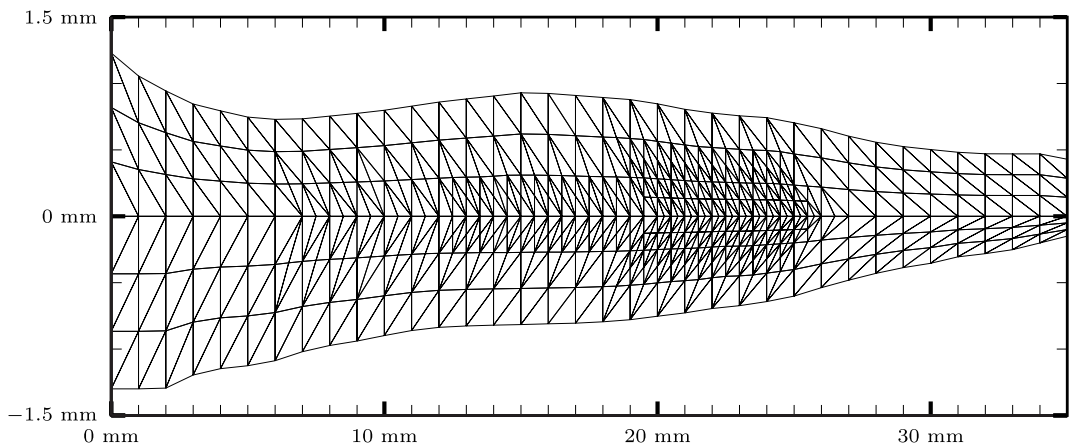

Fig. 5. The underlying mesh, used for the finite element analysis, is generated on the basis of an heuristic approach. The mesh is characterized by a gradual increase of its density along the basilar membrane until a point is reached where the traveling wave will probably be dissipated.

3.2. *Spatial discretization*

3.2.1. *The first-order system*

The finite element method is based on the *variational formulation* of the boundary value problem. The derivation of the variational formulation can be divided into three steps. In the first step, the partial differential equations of the boundary value problem must be multiplied by *test-functions* which are in agreement with the respective boundary-conditions. After that, the resultant statements must be integrated over the domain of interest. Finally, the requirements concerning the differentiability of individual field variables should, if possible, be weakened by applying *Green's first identity*.

Acoustic Subproblem: The weak form of the first-order equation of the conservation of momentum is given by

$$\rho^{(0)} \int_\Omega \bar{v}_i \frac{\partial v_i^{(1)}}{\partial t}\, d\boldsymbol{x} + \int_\Omega \frac{\partial \bar{v}_i}{\partial x_j} \sigma_{ij}^{(1)}\, d\boldsymbol{x} - \int_\Gamma \bar{v}_i \sigma_{ij}^{(1)} n_j\, dx = 0, \tag{24}$$

where the line above a variable indicates the test-functions. Due to the boundary condition (8), the boundary integral vanishes. According to the specification of the stress tensor (3), the second integral can be expanded to

$$\begin{aligned} \int_\Omega \frac{\partial \bar{v}_i}{\partial x_j} \sigma_{ij}^{(1)}\, d\boldsymbol{x} = \eta \int_\Omega \frac{\partial \bar{v}_i}{\partial x_j} \left(\frac{\partial v_i^{(1)}}{\partial x_j} + \frac{\partial v_i^{(1)}}{\partial x_i} \right) d\boldsymbol{x} \\ + \left(\zeta - \frac{2}{3}\eta \right) \int_\Omega \delta_{ij} \frac{\partial \bar{v}_i}{\partial x_j} \frac{\partial v_k^{(1)}}{\partial x_k}\, d\boldsymbol{x} - \int_\Omega \delta_{ij} \frac{\partial \bar{v}_i}{\partial x_j} p^{(1)}\, d\boldsymbol{x}. \end{aligned} \tag{25}$$

In this work, the two components of the velocity field as well as its first time derivatives are represented by quadratic finite element functions Q_i^Ω which are based on the well-known *Lagrange interpolation polynomials*. Therefore, the individual velocity components can be approximated by

$$\begin{aligned} v_1^{(1)} &\approx \hat{\mathbf{v}}_1^{(1)} \cdot \mathbf{Q}^\Omega = \hat{v}_{1,i}^{(1)} Q_i^\Omega, \quad & v_2^{(1)} &\approx \hat{\mathbf{v}}_2^{(1)} \cdot \mathbf{Q}^\Omega = \hat{v}_{2,i}^{(1)} Q_i^\Omega, \\ \dot{v}_1^{(1)} &\approx \dot{\hat{\mathbf{v}}}_1^{(1)} \cdot \mathbf{Q}^\Omega = \dot{\hat{v}}_{1,i}^{(1)}\, Q_i^\Omega, \quad & \dot{v}_2^{(1)} &\approx \dot{\hat{\mathbf{v}}}_2^{(1)} \cdot \mathbf{Q}^\Omega = \dot{\hat{v}}_{2,i}^{(1)}\, Q_i^\Omega, \end{aligned} \tag{26}$$

where the hat-symbol above a variable refers to a nodal vector. In order to ensure the stability of the mixed formulation, the so-called *Ladyzhenskaya–Babuska–Brezzi* (LBB) condition has to be fulfilled by the finite element spaces. With respect to the interpolation functions of the Lagrange family, it was shown that the polynomial degree of the basis functions, used to represent the pressure field, should be at least one order lower than the respective basis functions of the velocity components.[14] Therefore, the scalar pressure field as well as its time-derivative are represented by linear interpolation polynomials L_i^Ω belonging to the

Lagrange family:

$$p^{(1)} \approx \hat{\mathbf{p}}^{(1)} \cdot \mathbf{L}^{\Omega} = \hat{p}_i^{(1)} L_i^{\Omega}, \quad \dot{p}^{(1)} \approx \dot{\hat{\mathbf{p}}}^{(1)} \cdot \mathbf{L}^{\Omega} = \dot{\hat{p}}_i^{(1)} L_i^{\Omega}. \tag{27}$$

The variational formulation can now be transformed into its semi-discretized counterpart by substituting the finite element approximations for the respective field function. In addition, the test functions can also be replaced by individual basis functions. Having regard only to the terms that make a contribution to the first velocity component, the semi-discretized formulation can be written as

$$\begin{aligned}
&\left[\rho^{(0)} \int_{\Omega} Q_i^{\Omega} Q_j^{\Omega} \, d\boldsymbol{x}\right] \dot{\hat{v}}_{1,j}^{(1)} + \left[\int_{\Omega} \frac{\partial Q_i^{\Omega}}{\partial x_1} L_j^{\Omega} \, d\boldsymbol{x}\right] \hat{p}_j^{(1)} \\
&\quad + \left[\left(\zeta + \frac{4}{3}\eta\right) \int_{\Omega} \frac{\partial Q_i^{\Omega}}{\partial x_1} \frac{\partial Q_j^{\Omega}}{\partial x_1} \, d\boldsymbol{x} + \eta \int_{\Omega} \frac{\partial Q_i^{\Omega}}{\partial x_2} \frac{\partial Q_j^{\Omega}}{\partial x_2} \, d\boldsymbol{x}\right] \hat{v}_{1,j}^{(1)} \\
&\quad + \left[\left(\zeta - \frac{2}{3}\eta\right) \int_{\Omega} \frac{\partial Q_i^{\Omega}}{\partial x_1} \frac{\partial Q_j^{\Omega}}{\partial x_2} \, d\boldsymbol{x} + \eta \int_{\Omega} \frac{\partial Q_i^{\Omega}}{\partial x_2} \frac{\partial Q_j^{\Omega}}{\partial x_1} \, d\boldsymbol{x}\right] \hat{v}_{2,j}^{(1)} = 0.
\end{aligned} \tag{28}$$

For reasons of convenience, this system of equations can also be expressed in terms of a matrix-vector-notation as

$$\tilde{\mathbf{H}}^{v_1 v_1} \dot{\hat{\mathbf{v}}}_1^{(1)} + \tilde{\mathbf{K}}^{v_1 v_1} \hat{\mathbf{v}}_1^{(1)} + \tilde{\mathbf{K}}^{v_1 v_2} \hat{\mathbf{v}}_2^{(1)} + \tilde{\mathbf{K}}^{v_1 p} \hat{\mathbf{p}}^{(1)} = \mathbf{0}. \tag{29}$$

It must be noted that, up to now, the discretization process of the variational formulation does not ensure that the solution is in conformity with the respective boundary conditions. The Dirichlet condition can now be taken into account by modifying all rows of the matrices that are associated with a Dirichlet node. If I denotes the set that contains all Dirichlet nodes with respect to the first velocity component and if I_{ow} is a subset of I that includes only the nodes at the oval window, a modified version of the matrix $\tilde{\mathbf{K}}^{v_1 v_1}$ as well as a new right-hand vector can be specified as

$$\mathrm{K}_{ij}^{v_1 v_1} = \begin{cases} \delta_{ij} & \text{if } \; i \in I, \\ \tilde{\mathrm{K}}_{ij}^{v_1 v_1} & \text{otherwise}, \end{cases} \qquad \mathrm{F}_i^{v_1} = \begin{cases} \dfrac{\partial \xi_{\mathrm{ow}}(\boldsymbol{x})}{\partial t} & \text{if } \; i \in I_{\mathrm{ow}}, \\ 0 & \text{otherwise}. \end{cases} \tag{30}$$

with δ_{ij} being the *Kronecker delta operator*. The final semi-discretized formulation that also takes the boundary condition into account can now be expressed as

$$\mathbf{H}^{v_1 v_1} \dot{\hat{\mathbf{v}}}_1^{(1)} + \mathbf{K}^{v_1 v_1} \hat{\mathbf{v}}_1^{(1)} + \mathbf{K}^{v_1 v_2} \hat{\mathbf{v}}_2^{(1)} + \mathbf{K}^{v_1 p} \hat{\mathbf{p}}^{(1)} = \mathbf{F}^{v_1}, \tag{31}$$

where the matrices $\mathbf{H}^{v_1 v_1}$, $\mathbf{K}^{v_1 v_2}$ and $\mathbf{K}^{v_1 p}$ arises from erasing all entries of the preliminary matrices that belong to a Dirichlet row $i \in I$. In a similar way, the discretization process of

the first-order Eq. (11) also induces a second system of equation which can be represented as

$$\mathbf{H}^{v_2v_2}\dot{\hat{\mathbf{v}}}_2^{(1)} + \mathbf{K}^{v_2v_1}\hat{\mathbf{v}}_1^{(1)} + \mathbf{K}^{v_2v_2}\hat{\mathbf{v}}_2^{(1)} + \mathbf{K}^{v_2p}\hat{\mathbf{p}}^{(1)} + \mathbf{H}^{v_2\xi}\dot{\hat{\boldsymbol{\xi}}} = \mathbf{0}. \tag{32}$$

In contrast to the first system, the second system is supplemented by the matrix $\mathbf{H}^{v_2\xi}$, which is needed to specify the Dirichlet condition at the cochlear partition in dependence of the first time-derivative of the basilar membrane displacement represented by the nodal vector $\dot{\hat{\boldsymbol{\xi}}}$. This is possible because each boundary node at the top or the bottom of the cochlear partition that belongs to the fluid domain can be directly linked to a corresponding node on the basilar membrane due to the specific construction of the mesh.

Besides the discretized first-order equation that originates from the conservation of linear momentum, the first-order equation that represents the mass balance has also to be taken into account in order to describe the acoustic reaction within the fluid domain. On the basis of its weak formulation, the semi-discretized formulation of the mass balance can be evaluated to

$$\mathbf{H}^{pp}\dot{\hat{\mathbf{p}}}^{(1)} + \mathbf{K}^{pv_1}\hat{\mathbf{v}}_1^{(1)} + \mathbf{K}^{pv_2}\hat{\mathbf{v}}_2^{(1)} = 0. \tag{33}$$

Dynamics of the Basilar Membrane: According to the differential equation (14), the semi-discretized system that simulates the displacement of the basilar membrane can be determined to

$$\mathbf{M}^{\xi\xi}\ddot{\hat{\boldsymbol{\xi}}} + \mathbf{H}^{\xi\xi}\dot{\hat{\boldsymbol{\xi}}} + \mathbf{K}^{\xi\xi}\hat{\boldsymbol{\xi}} + \mathbf{K}^{\xi p}\hat{\mathbf{p}}^{(1)} + \mathbf{K}^{\xi\zeta}\hat{\boldsymbol{\zeta}} = \mathbf{0}. \tag{34}$$

The internal physical properties of the basilar membrane are described by the mass matrix $\mathbf{M}^{\xi\xi}$, the damping matrix $\mathbf{H}^{\xi\xi}$ and the stiffness matrix $\mathbf{K}^{\xi\xi}$. The displacement is caused by the pressure difference across cochlear partition. This external pressure load can be calculated with the help of the matrix $\mathbf{K}^{\xi p}$. Finally, the force exerted by outer hair cell motility can evaluated by using the matrix $\mathbf{K}^{\xi\zeta}$.

As described in Sec. 2.2.3, the deflections of the hair-bundles are modeled as an additional array of sub-oscillators. The stiffness, the damping and the mass properties are reflected in the matrices $\mathbf{K}^{\zeta\zeta}$, $\mathbf{H}^{\zeta\zeta}$ and $\mathbf{M}^{\zeta\zeta}$. This sub-oscillator is stimulated by the displacement of the basilar membrane and the resultant coupling is realized by the matrix $\mathbf{M}^{\zeta\xi}$. By the use of these matrices, the variational formulation of Eq. (18) can be transformed into the ordinary differential equation

$$\mathbf{M}^{\zeta\zeta}\ddot{\hat{\boldsymbol{\zeta}}} + \mathbf{H}^{\zeta\zeta}\dot{\hat{\boldsymbol{\zeta}}} + \mathbf{K}^{\zeta\zeta}\hat{\boldsymbol{\zeta}} + \mathbf{M}^{\zeta\xi}\ddot{\hat{\boldsymbol{\xi}}} = \mathbf{0}. \tag{35}$$

The dynamics of the basilar membrane are calculated on the basis of one-dimensional linear interpolation functions that belong to the Lagrange family.

3.2.2. *Multiphysical coupling*

In principle, two different approaches for the numerical implementation of a multiphysical problem can be distinguished. The first approach for simulating multiple processes involves

the consideration of the coupled processes as one monolithic system of equations. The major drawback of this procedure is that the resultant system of equations may become quite large and its associated matrix is potentially badly conditioned. In contrast, the second approach is based on separate sub-routines that are specialized in the numerical computation of the different physical phenomena that are involved. In this case, the coupling is realized by the transfer of relevant data that can be taken into account by specific boundary conditions, load terms, geometric shape or constitutive relations.[14,26]

In this work, the multiphysical problem is realized by a monolithic system of equations. It can be assumed that a partitioned realization of the coupling involves a substantial computational effort that is probably needed by the application of sub-iterations due to the strong interdependence between the fluid, the basilar membrane and the outer hair cell motility. Therefore, it cannot be expected that the partitioned implementation has significant advantages with respect to the computational effort over a monolithic realization. Furthermore, the modular design is accompanied with a substantial increase of the code complexity, due to the additional implementation of adequate interfaces, data transfer protocols, finite element interpolations and the monitoring of the sub-iteration processes.

According to Eqs. (31)–(35), the fully coupled monolithic system of the first-order acoustic subproblem can be represented as

$$\mathbf{M}\ddot{\mathbf{u}} + \mathbf{H}\dot{\mathbf{u}} + \mathbf{K}\mathbf{u} = \mathbf{F} \tag{36}$$

which constitutes a system of second-order linear ordinary differential equations. The nodal vector $\mathbf{u}$ combines the individual nodal vectors of the fluid velocity, fluid pressure, basilar membrane displacement and hair-bundle deflection and this overall vector can be written as

$$\mathbf{u} = [\hat{\mathbf{v}}_1^{(1)} \hat{\mathbf{v}}_2^{(1)} \hat{\mathbf{p}}^{(1)} \hat{\boldsymbol{\xi}} \hat{\boldsymbol{\zeta}}]^T. \tag{37}$$

Due to the similarity of Eq. (36) to equations of motions where the vector $\mathbf{u}$ is usually identified with the displacement of the motion, the matrices $\mathbf{M}$, $\mathbf{H}$ and $\mathbf{K}$ are often referred to as the mass matrix, the damping matrix and the stiffness matrix. By using the sub-matrices of the individual equations as introduced above, the stiffness matrix can be given as

$$\mathbf{K} = \begin{bmatrix} \mathbf{K}^{v_1 v_1} & \mathbf{K}^{v_1 v_2} & \mathbf{K}^{v_1 p} & \mathbf{0} & \mathbf{0} \\ \mathbf{K}^{v_2 v_1} & \mathbf{K}^{v_2 v_2} & \mathbf{K}^{v_2 p} & \mathbf{0} & \mathbf{0} \\ \mathbf{K}^{p v_1} & \mathbf{K}^{p v_2} & \mathbf{0} & \mathbf{0} & \mathbf{0} \\ \mathbf{0} & \mathbf{0} & \mathbf{K}^{\xi p} & \mathbf{K}^{\xi\xi} & \mathbf{K}^{\xi\zeta} \\ \mathbf{0} & \mathbf{0} & \mathbf{0} & \mathbf{0} & \mathbf{K}^{\zeta\zeta} \end{bmatrix}. \tag{38}$$

The discretized damping matrix of the first-order subproblem can be represented as

$$\mathbf{H} = \begin{bmatrix} \mathbf{H}^{v_1 v_1} & \mathbf{0} & \mathbf{0} & \mathbf{0} & \mathbf{0} \\ \mathbf{0} & \mathbf{H}^{v_2 v_2} & \mathbf{0} & \mathbf{H}^{v_2 \xi} & \mathbf{0} \\ \mathbf{0} & \mathbf{0} & \mathbf{H}^{pp} & \mathbf{0} & \mathbf{0} \\ \mathbf{0} & \mathbf{0} & \mathbf{0} & \mathbf{H}^{\xi\xi} & \mathbf{0} \\ \mathbf{0} & \mathbf{0} & \mathbf{0} & \mathbf{0} & \mathbf{H}^{\zeta\zeta} \end{bmatrix}. \tag{39}$$

Finally, the overall mass matrix can be determined to

$$\mathbf{M} = \begin{bmatrix} \mathbf{0} & \mathbf{0} & \mathbf{0} & \mathbf{0} & \mathbf{0} \\ \mathbf{0} & \mathbf{0} & \mathbf{0} & \mathbf{0} & \mathbf{0} \\ \mathbf{0} & \mathbf{0} & \mathbf{0} & \mathbf{0} & \mathbf{0} \\ \mathbf{0} & \mathbf{0} & \mathbf{0} & \mathbf{M}^{\xi\xi} & \mathbf{0} \\ \mathbf{0} & \mathbf{0} & \mathbf{0} & \mathbf{M}^{\zeta\xi} & \mathbf{M}^{\zeta\zeta} \end{bmatrix}. \tag{40}$$

By the monolithic matrix representation, the interdependencies between different field variables are easily recognizable by the sub-matrices that are not located on the main diagonal.

The right-hand side of the first-order semi-discretized formulation consists only of entries belonging to the first velocity components that are associated with the displacement of the oval window. Therefore, the load vector can be written as

$$\mathbf{F} = [\mathbf{F}^{v_1}\ \mathbf{0}\ \mathbf{0}\ \mathbf{0}\ \mathbf{0}]^T. \tag{41}$$

3.2.3. *The second-order system*

The spatial discretization of the acoustic streaming subproblem, which consists of the differential equations (19) and (21), can be performed on the basis of their respective variational formulation. The resultant time-independent system of equations can be written in terms of a mixed formulation as

$$\begin{bmatrix} \mathbf{G}^{v_1 v_1} & \mathbf{G}^{v_1 v_2} & \mathbf{G}^{v_1 p} \\ \mathbf{G}^{v_2 v_1} & \mathbf{G}^{v_2 v_2} & \mathbf{G}^{v_2 p} \\ \mathbf{G}^{p v_1} & \mathbf{G}^{p v_2} & \mathbf{G}^{pp} \end{bmatrix} \begin{bmatrix} \hat{\mathbf{v}}_1^{(dc)} \\ \hat{\mathbf{v}}_2^{(dc)} \\ \hat{\mathbf{p}}^{(dc)} \end{bmatrix} = \begin{bmatrix} \mathbf{S}^{v_1} \\ \mathbf{S}^{v_2} \\ \mathbf{S}^{p} \end{bmatrix}. \tag{42}$$

The force-source distribution as well as the mass-source distribution are taken into account by the load vector at the right-hand side.

3.3. *Temporal discretization*

This work uses an approach that was originally suggested by Houbolt.[27] The approximation technique from Houbolt is a second-order method, which means that the error per

time-step is of the order Δt^2. Furthermore, the scheme is numerically stable since it is an implicit approach.[28] The integration scheme from Houbolt uses the following backward finite difference approximations for the first and second time-derivative:

$$\dot{\mathbf{u}}_{t+\Delta t} = -\frac{1}{6\Delta t}\left(2\mathbf{u}_{t-2\Delta t} - 9\mathbf{u}_{t-\Delta t} + 18\mathbf{u}_t - 11\mathbf{u}_{t+\Delta t}\right), \tag{43}$$

$$\ddot{\mathbf{u}}_{t+\Delta t} = -\frac{1}{\Delta t^2}\left(\mathbf{u}_{t-2\Delta t} - 4\mathbf{u}_{t-\Delta t} + 5\mathbf{u}_t - 2\mathbf{u}_{t+\Delta t}\right). \tag{44}$$

The semi-discretized formulation of the first-order problem at time $t + \Delta t$ can be written as

$$\mathbf{M}\ddot{\mathbf{u}}_{t+\Delta t} + \mathbf{H}\dot{\mathbf{u}}_{t+\Delta t} + \mathbf{K}\mathbf{u}_{t+\Delta t} = \mathbf{F}_{t+\Delta t}. \tag{45}$$

By substituting the approximations (43) and (44) for the velocity-like vector $\dot{\mathbf{u}}_{t+\Delta t}$ and the acceleration-like vector $\ddot{\mathbf{u}}_{t+\Delta t}$, the fully discretized first-order subproblem can be represented by the simple linear system of equations

$$\mathbf{A}\mathbf{u}_{t+\Delta t} = \mathbf{b}. \tag{46}$$

In this context, the matrix $\mathbf{A}$ can be evaluated as

$$\mathbf{A} = \frac{2}{\Delta t^2}\mathbf{M} + \frac{11}{6\Delta t}\mathbf{H} + \mathbf{K}. \tag{47}$$

As it can be seen, it is sufficient to determine the matrix $\mathbf{A}$ only once at the beginning of the numerical time integration process due to the stationary character of the mass matrix $\mathbf{M}$, the damping matrix $\mathbf{H}$ and the stiffness matrix $\mathbf{K}$. The load term $\mathbf{b}$ can be calculated as

$$\begin{aligned}\mathbf{b} = &\left(\frac{1}{\Delta t^2}\mathbf{M} + \frac{1}{3\Delta t}\mathbf{H}\right)\mathbf{u}_{t-2\Delta t} - \left(\frac{4}{\Delta t^2}\mathbf{M} + \frac{3}{2\Delta t}\mathbf{H}\right)\mathbf{u}_{t-\Delta t} \\ &+ \left(\frac{5}{\Delta t^2}\mathbf{M} + \frac{3}{\Delta t}\mathbf{H}\right)\mathbf{u}_t + \mathbf{F}_{t+\Delta t}.\end{aligned} \tag{48}$$

In contrast to the stationary matrix on the left-hand side of Eq. (46), the load term $\mathbf{b}$ has to be updated at each time-step due to the dependency on the time-varying load vector $\mathbf{F}_{t+\Delta t}$ (which takes account of the predefined displacements of the oval window) and the inclusion of the state vectors $\mathbf{u}$ at the preceding three time-steps.

3.4. *Solver*

The discretization process of the first-order system results in a sequence of linear systems of equations (cf. (46)). Under the assumption of a constant time-step, the linear systems are characterized by a constant, large, sparse and nonsymmetric matrix as well as a time-varying right-hand side vector. In order to get a numerical solution of each system, the *generalized*

minimal residual method (GMRES) is used due to its applicability for nonsymmetric systems. The iterative GMRES approach was originally developed by Saad and Schultz[29] and it is based on a projection method, which approximates the solution within the so-called *Krylov subspace*.

The acoustically driven flow field can be achieved by solving the symmetric system of equations as described in Sec. 3.2.3. Although the symmetry of the matrix allows the usage of more efficient methods (e.g. the *Lanczos algorithm*), the GMRES method is also used for solving the mean second-order system.

The speed of convergence of an iterative solver (like GMRES) can be significantly enhanced by transforming the linear system of equations into a better conditioned system. In this work, this preconditioning is performed by the use of the *incomplete LU decomposition*.[30]

4. Results

In this section, the numerical results of the computational model, introduced in this work, are presented. In order to ensure the correct functionality of the model, the numerical results are compared to experimental studies, measurements and analytical estimates.

4.1. *Harmonic stimulation of the first-order system*

The accuracy of the first-order system is crucial for the correctness of the results of the second-order system, which provides estimations for the occurrence of acoustically driven flows within the inner ear. Therefore, the first part is concerned with an accurate verification of this acoustic system. It is analyzed under an harmonic stimulation of the oval window at different frequencies and amplitudes. Furthermore, the system is examined both in the active case, where the outer hair cell motility is taken into account, and in the passive case without any motility driven forces.

Particular attention is paid to the equilibrium state of the first-order system, since it is the basis for the numerical calculation of acoustic streaming. This steady state is achieved within a short time frame. According to Köster,[6] the equilibrium state of the fluid can be expressed by harmonic oscillations of the individual field variables at fixed positions. In terms of sin- and cos-functions, the stable state of the velocity field, for example, can be written as

$$\boldsymbol{v}^{(1)}(\boldsymbol{x},t) = \boldsymbol{v}^{(\sin)}(\boldsymbol{x})\sin(\omega t) + \boldsymbol{v}^{(\cos)}(\boldsymbol{x})\cos(\omega t). \tag{49}$$

Therefore, the oscillatory motion of the fluid can be uniquely characterized by the time-independent functions $\boldsymbol{v}^{(\sin)}(\boldsymbol{x})$ and $\boldsymbol{v}^{(\cos)}(\boldsymbol{x})$.

Today, it is well accepted that the motions of the basilar membrane can be characterized on the basis of a typical *traveling wave* pattern. The resultant displacements in comparison to the traveling wave pattern of the cochlear partition are reviewed in the first part. Furthermore, it has been shown that some boundary layer effects are mainly responsible for

acoustically driven flows. In the second part, the motion within this thin boundary layer is therefore compared with an analytical approximation developed by Lighthill.[2]

4.1.1. *Traveling wave on the basilar membrane*

The term "traveling wave" is associated with a characteristic displacement pattern of the cochlear partition. This pattern is characterized by the following properties[22,31]:

- The amplitude of the traveling wave increases until a point of maximal displacement (peak) is reached. Often, this location is referred to as *characteristic place*. Behind this place, the amplitude falls to zero within a short distance.
- The phase of the oscillatory displacements decreases monotonically along the basilar membrane. This phase lag may amount to up to several cycles until the traveling wave dissipates.
- The traveling wave is caused by (passive) mechanical interactions between the fluid and the structures of the cochlea. This means that the traveling wave is, in particular, not a result of any other internal (physiological) processes.
- In contrast to the acoustic waves, which propagate at speeds of about 1500 m/s, the velocity of the traveling wave motion of the basilar membrane is significantly slower.

Passive Cochlea Model: Figure 8 shows the envelopes and phases of the traveling waves of the basilar membrane in the passive case. The sound field is driven by the sinusoidal displacement of the oval window (cf. Fig. 2) at stimulation frequencies of 128, 256, 512, 1024, 2048, 4096 and 8192 Hz. The displacement pattern of the cochlear partition is exemplarily illustrated in Fig. 7(a). It becomes apparent that the resultant displacements of the cochlear partition meet the requirements of the typical traveling wave motion as described above. The phase lag adds up to just under four cycles at the lower frequencies and increases to more than five cycles at higher frequencies.

As it can be clearly seen, the longitudinal position of the characteristic place depends mainly on the frequency. Greenwood[25] empirically developed a functional relationship that assigns the characteristic places to their corresponding stimulation frequency. With regard to the human cochlea this frequency-position map is given by

$$f = 350 \cdot (10^{\frac{2.1}{l_{\mathrm{bm}}}(x - l_{\mathrm{bm}})} - 0.85), \tag{50}$$

where l_{bm} denotes the length of the basilar membrane. Figure 9 shows that the maximal displacements of the traveling wave are located up to about 5 mm closer to the base in the passive cochlea model than in the case of Greenwood's examination.

Active Cochlea Model: The passive behavior represents only the mechanics of a dead cochlea. As it can be seen in Fig. 10, the dynamics of the living ear are quite different to those of a postmortem cochlea.

First of all, it can be noted that the amplification of the traveling wave motion is accompanied by a spatial shift of the peak in the direction of the apex. Such a shift is

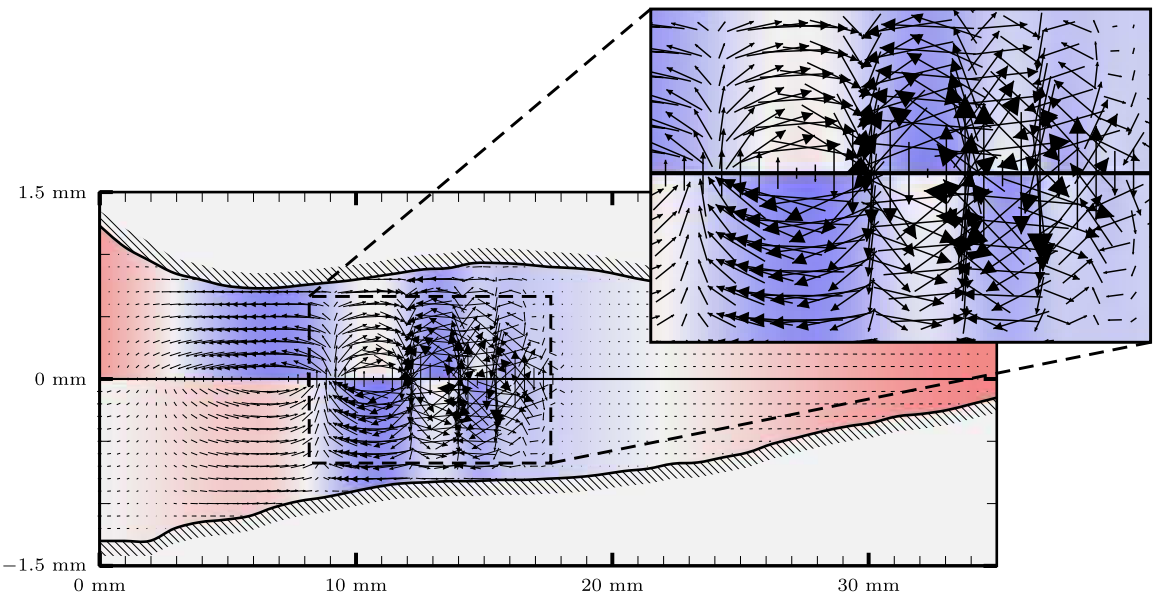

(a)

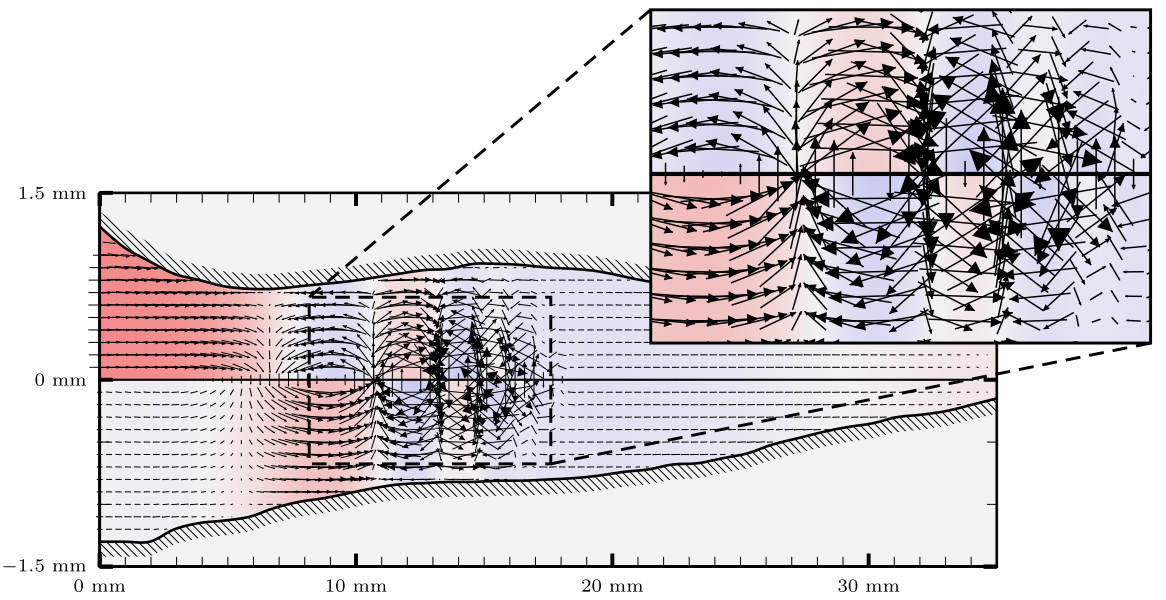

(b)

Fig. 6. (Color online) Equilibrium state of the first-order system at a stimulation frequency of 1024 Hz in the passive cochlea model. The vector field of (a) illustrates the cosine-component $v^{(\cos)}$ of the first-order velocity field, whereas the background color is associated with the cosine-part $p^{(\cos)}$ of the first-order pressure field. In this context, the intensity of the red (blue) color represents the amount of the positive (negative) excess pressure. In contrast, (b) illustrates the respective sine components $v^{(\sin)}$ and $p^{(\sin)}$.

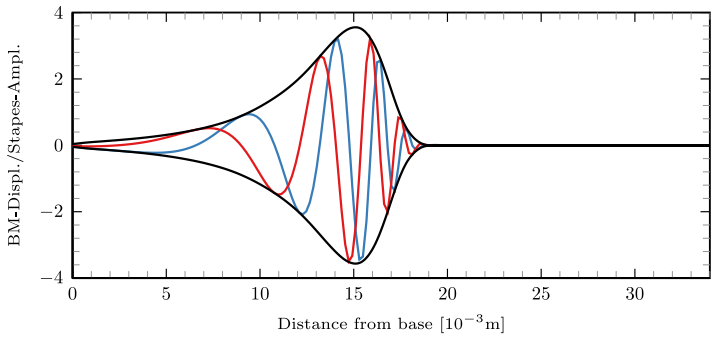

(a)

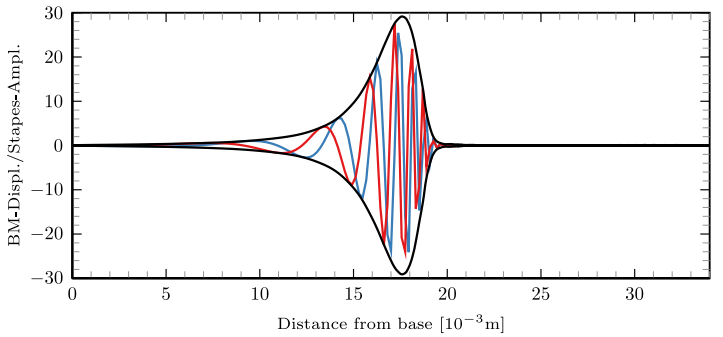

(b)

Fig. 7. (Color online) Traveling wave motion of the basilar membrane at a stimulation frequency of 1024 Hz in the passive (a) and active (b) cochlea model. The red line represents the cosine part $\xi^{(\cos)}$ of the oscillatory motion, whereas the blue line is associated with the sine component $\xi^{(\sin)}$. The black line illustrates the envelope.

mostly consistent with experimental studies. It is an indication that the energy of the traveling wave motion is enhanced by the outer hair cells.[22] Therefore, the characteristic places are closer to the functional relationship from Greenwood than in the passive case (cf. Fig. 9).

It can be clearly seen that the maximal displacement of the basilar membrane is increased up to the ten-fold of the maximal displacement in the passive case. In literature different definitions of the cochlear amplifier gain are used.[22] In this paper, the gain is understood as the difference between the amplitudes of the active and the passive cochlea at the same locations on the basilar membrane. Within the cochlea of the guinea pig, gains between 65 dB and 78 dB were measured at the characteristic places of frequencies between 17 kHz and 19 kHz.[32–35] As shown in Fig. 11, such a gain of the amplitude cannot be completely reproduced by the computational model presented in this work. Nevertheless, the model presented in this work provides an instrument to investigate the effects of the amplification mechanisms on the resultant acoustically driven flows. On the basis of these results, further conclusions may be drawn with regard to the impact of acoustic streaming at even higher gains.

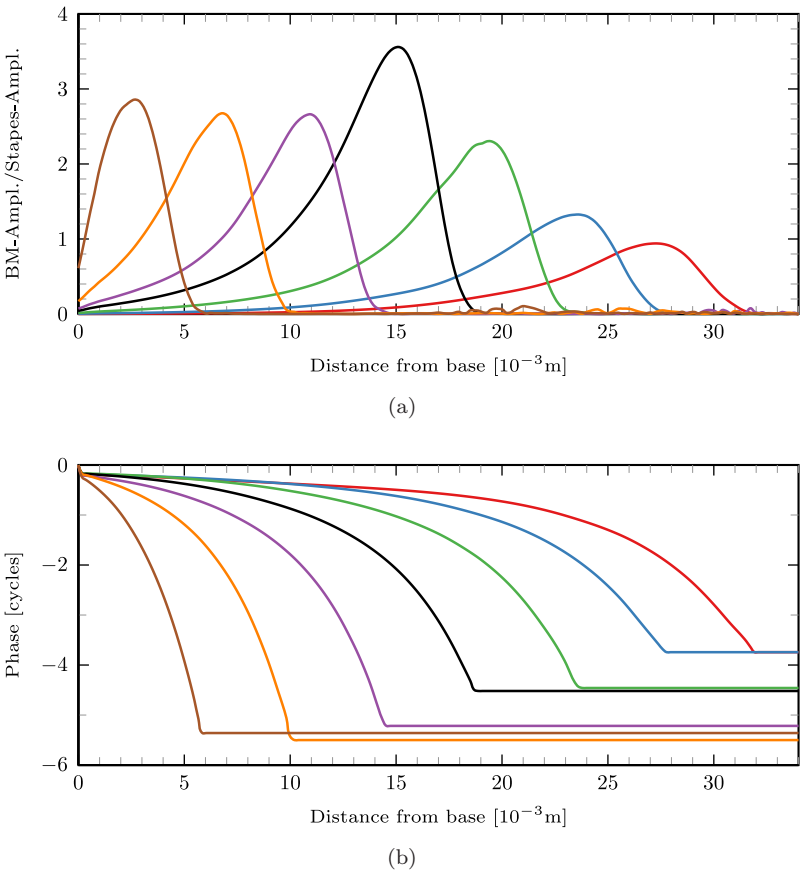

Fig. 8. (Color online) Envelopes (a) and phases (b) of the traveling wave in the passive cochlea model computed at constant stape displacement for a set of different frequencies: 128 (red line), 256 (blue line), 512 (green line), 1024 (black line), 2048 (purple line), 4096 (orange line) and 8192 Hz (brown line).

In addition, the traveling wave is characterized by a higher phase lag than in the passive cochlea model (cf. Fig. 10(b)). In consideration of the envelopes (cf. Fig. 10(a)) it can be seen that the respective shapes in the active model are significantly sharper than in the passive case. This property of the amplification mechanism is believed to be a very important aspect with respect to the acoustic perception, because it enhances the frequency selectivity.

4.1.2. *Motions within the stokes boundary layer*

Because the dissipation of acoustic energy within the thin *Stokes boundary layer* next to the basilar membrane is a major cause for second-order flows, particular attention has to be paid to an accurate numerical approximation of the motions within these boundary layers. The results of the computational model presented in this work can be validated by comparing the numerically determined motions with some theoretical considerations from Lighthill.[2] In his very important contribution, Lighthill estimated the dimension of acoustic streaming within the inner ear on the basis of a mathematical description of the flow field adjacent to

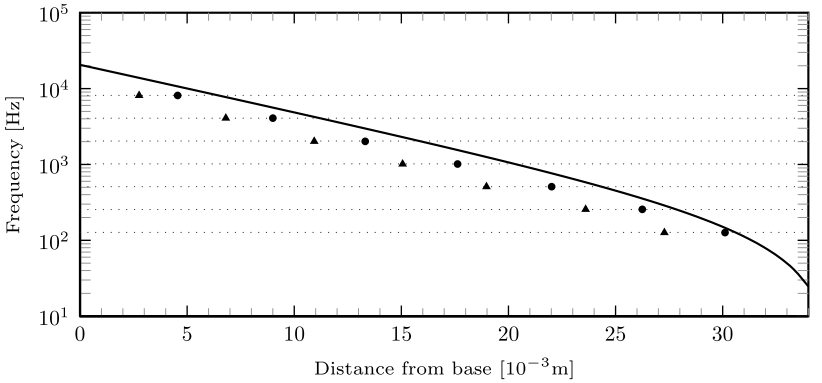

Fig. 9. The frequency-position map (solid line) from Greenwood[25] assigns the characteristic places to their corresponding stimulation frequency. The triangles illustrate the characteristic places resulting from the passive cochlea model whereas the dots represent the characteristic places in the active case.

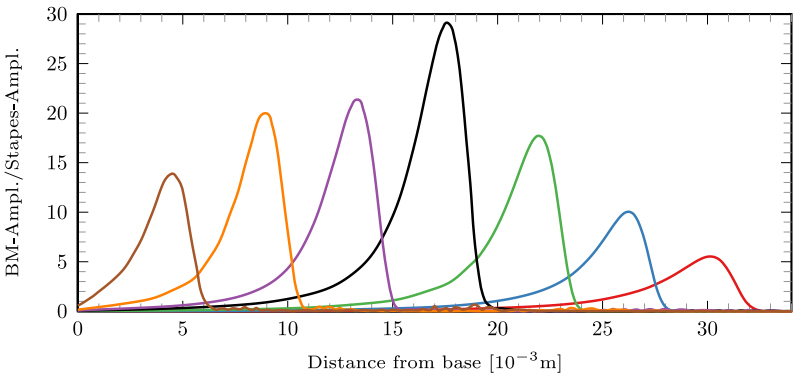

(a)

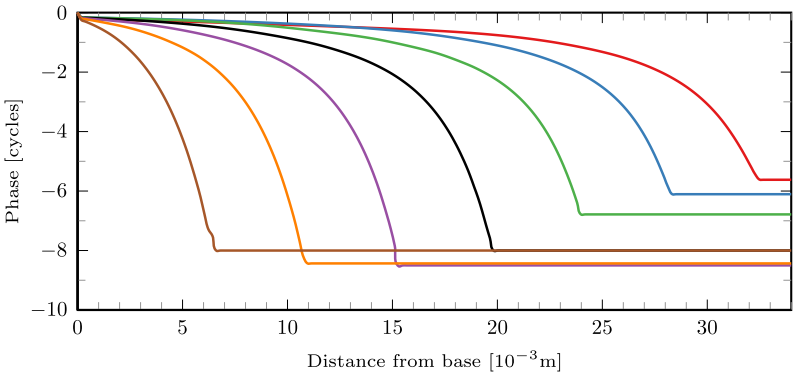

(b)

Fig. 10. (Color online) Envelopes (a) and phases (b) of the traveling wave in the active cochlea model computed at constant stape displacement for a set of different frequencies: 128 (red line), 256 (blue line), 512 (green line), 1024 (black line), 2048 (purple line), 4096 Hz (orange line) and 8192 Hz (brown line).

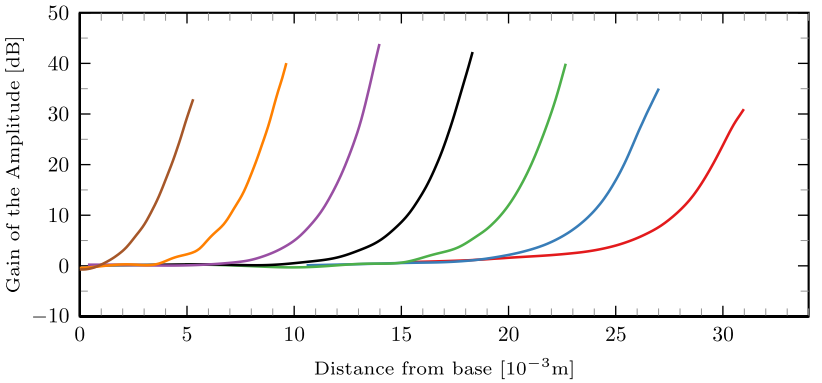

Fig. 11. (Color online) Positional gain of the envelopes at different frequencies in the active cochlea model with respect to the envelopes in the passive cochlea model: 128 (red line), 256 (blue line), 512 (green line), 1024 (black line), 2048 (purple line), 4096 (orange line) and 8192 Hz (brown line).

the basilar membrane. In this context, he suggested to approximate the three-dimensional distribution of the fluid motion next to the traveling wave of the basilar membrane by the superposition of solutions of the Laplace equation

$$\frac{\partial^2 \phi}{\partial x_2^2} + \frac{\partial^2 \phi}{\partial x_3^2} - k^2 \phi = 0, \tag{51}$$

where ϕ denotes the velocity potential. By the use of the so-called WKB method (also known as Liouville–Green method), Lighthill reasoned that the fluid motion outside of a thin boundary layer of the basilar membrane near to the characteristic place can be mainly approximated by a two-dimensional circular motion perpendicular to the radial axis. In terms of a mathematical formulation, this motion can be written as

$$v_1 = \frac{\partial \phi}{\partial x_1} = \mathrm{i}\xi \mathrm{e}^{-kx_2}, \tag{52}$$

$$v_2 = \frac{\partial \phi}{\partial x_2} = \xi \mathrm{e}^{-kx_2}. \tag{53}$$

But in order to meet the no-slip boundary conditions at the basilar membrane, Eqs. (52) and (53) have to be adapted according to *Rayleigh's law of streaming*,[36] yielding

$$v_1 = \mathrm{i}\xi\left(1 - \mathrm{e}^{-x_2\sqrt{\mathrm{i}\omega\rho/\eta}}\right), \tag{54}$$

$$v_2 = \xi\left(1 + \left(1 - \mathrm{e}^{-x_2\sqrt{\mathrm{i}\omega\rho/\eta}}\right)\frac{\omega}{c}\sqrt{\frac{\eta}{\mathrm{i}\omega\rho}}\right). \tag{55}$$

Figure 12 shows the numerically determined motions within the thin boundary layer in comparison to the analytical results from Lighthill. The thickness of the boundary layer can

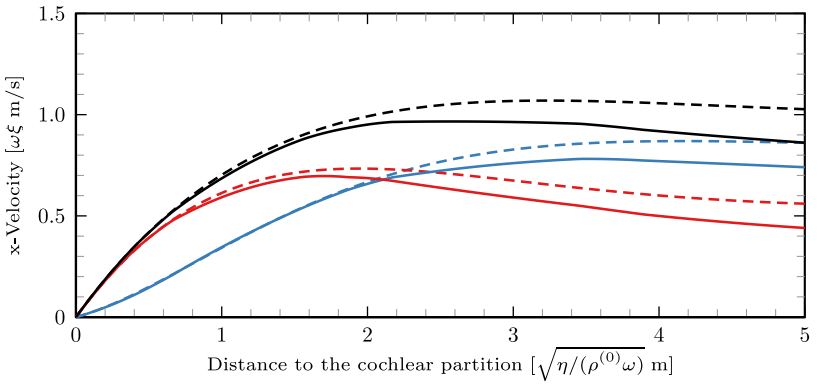

(a)

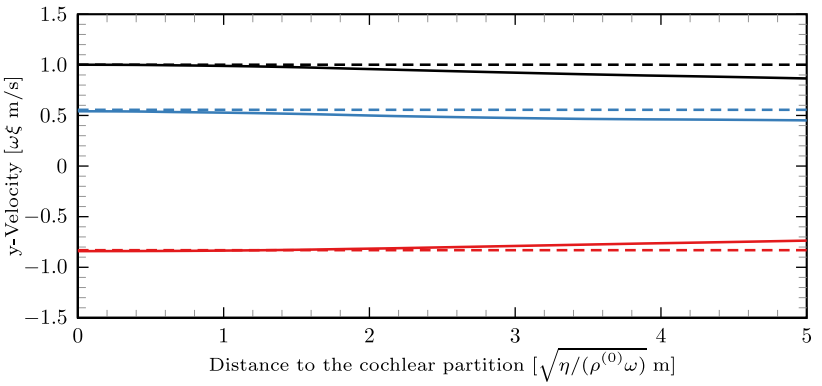

(b)

Fig. 12. (Color online) Comparison between the numerical results of the computational model (solid lines) presented in this work and the theoretical approximation (dashed lines) of the fluid motions within the Stokes boundary layer from Lighthill[2] near to the characteristic place at a stimulation frequency of 1024 Hz in the passive model. (a) illustrates the longitudinal velocity components whereas (b) shows the vertical components. The red, blue and black lines are associated with the cosine-part, the sine-part and the amplitude of the respective velocity component.

be approximately determined to $5\sqrt{\eta/\rho\omega}$. With regard to typical stimulation frequencies and the spatial dimensions of the cochlea, the Stokes boundary layer is comparatively small. Therefore, it is very important that the finite element discretization process constructs a mesh that is sufficiently small to ensure an adequate approximation of the velocity and pressure field. It can be noted that the motions close to the boundary are nearly identical. The greater the distance to the cochlear partition, the greater the deviation of the numerical results from the analytical approximations.

In consideration of the differences between both approaches, these deviations between the results seem to be relatively small. In contrast to the computational model presented here, Lighthill's model neglected the energy dissipation due to viscous forces within the bulk as well as some interference effects arising from the interaction with the solid boundaries.

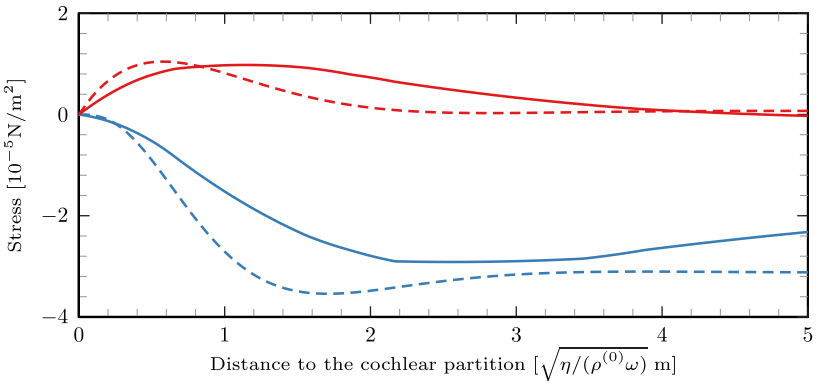

Fig. 13. (Color online) The graph illustrates the resultant Reynolds stresses of the computational model (solid lines) within in the Stokes boundary layer in comparison to theoretical approximations (dashed lines) from Lighthill.[2] The data originate from the characteristic place at a stimulation frequency of 1024 Hz with respect to the passive cochlea model. The red lines depict the shear stress component that describes the x_2-flux of x_1-momentum per unit area. In contrast, the blue lines are associated with the normal stress component that represents the x_1-flux of x_1-momentum per unit area.

In addition to this, by the use of the Laplace equation (51), Lighthill assumed that the motions can be described as an irrotational and incompressible flow. Otherwise, also the numerical evaluation has the well-known limitations in accuracy, based on the local resolution of the mesh, the choice of form-functions as well as other numerical effects. Whilst taking all these aspects into account, the computational model yields very good results when comparing the numerical results of the motion within the Stokes boundary layer with the analytical approximations from Lighthill.

4.2. *Fluid flows driven by the second-order system*

It was determined that the most important cause for acoustic streaming field can be associated with the forces within the thin boundary layer next to the basilar membrane. In the first part of this section, the stresses within this boundary layer are therefore compared with the analytical approximations from Lighthill.[2] In addition, the magnitude of the acoustically driven flow velocities are contrasted with his resultant estimates. The flow field arising from the mean second-order system is described and evaluated in the second part of this section. In this context, the flow field is also compared with experiments made by Tonndorf.[4]

4.2.1. *Force source driven streaming*

In order to understand the physical origin of the resulting forces, Bradley[7] pointed out that the force-source distribution, accurate to the second-order, can be written as the product of the fluid-acceleration $\boldsymbol{a} = \frac{\partial \boldsymbol{v}}{\partial t} + (\operatorname{grad} \boldsymbol{v})\boldsymbol{v}$ and the density:

$$\tilde{\boldsymbol{f}} = -\langle(\rho \boldsymbol{a})\rangle + \mathcal{O}(\epsilon^3). \tag{56}$$

Therefore, the force depends mainly on the phase between the fluid-acceleration and the density. The exerted force per unit volume $\tilde{\boldsymbol{f}}$ can also be represented in terms of the well-known *Reynolds stress* tensor, which can be expressed as $\rho v_i v_j$. By using integration by parts, the (first-order) mass conservation (cf. Eq. (10)) and the product rule, the force-source distribution can be written as the spatial variation of the Reynolds stress:

$$\tilde{\boldsymbol{f}} = -\rho^{(0)} \left\langle \frac{\partial v_i^{(1)} v_j^{(1)}}{\partial x_i} \right\rangle \boldsymbol{e}_j. \tag{57}$$

This force can furthermore be decomposed into a shear stress component and a normal stress component. The shear stress components describe the flux of momentum per unit area perpendicular to its orientation whereas the normal stress components are characterized by equal directions of the force and its flux.

The results of the experiments, performed by the computational model, show that the forces are predominant at the adjacent boundary layers of the basilar membrane near to the characteristic place. This observation is in conformity with the theoretical considerations from Lighthill[2] whose estimation of acoustic streaming is mainly based on the Reynolds stresses occurring within the Stokes boundary layer. In his work, he evaluated an effective slip velocity outside of the thin Stokes boundary layer. In terms of the velocity amplitude of the oscillating basilar membrane, this effective slip flow can be expressed as

$$\frac{\pi f k}{2} (\xi^{(\mathrm{amp})})^2 - \frac{3\pi f}{2} \xi^{(\mathrm{amp})} \frac{\partial \xi^{(\mathrm{amp})}}{\partial x_1}. \tag{58}$$

The first term as well as one-third of the second term originate from the shear stress component that transports the x_1-momentum in the x_2-direction. In contrast, two-thirds of the second summand can be attributed to the normal component of the Reynolds stress driven force. A detailed derivation of this slipping flow estimate can be found in the work from Lighthill.[2]

The formula from Lighthill can be used to calculate the effective slip velocity of acoustic streaming on the basis of the first-order field resulting from the computational model. The resultant maximal velocities are shown in Fig. 14(b). In turn, Fig. 14(a) illustrates the maximal mean velocities outside of the Stokes boundary layer that are calculated on the basis of the computational model. By comparing both results it can be noticed that the velocities of the computational model are up to one order of magnitude larger than Lighthill's estimates.

These discrepancies can mainly be traced back to the slight differences in the distribution of the Reynolds stress within the Stokes boundary layer. Figure 13 shows the numerically determined stresses in comparison to the stresses that are calculated on the basis of the velocity components (54) and (55) used by Lighthill. These deviations arises mainly from the differences with respect to the first-order velocity field (cf. Fig. 12). One reason for the discrepancy in the first-order flow field lies in the quite different underlying assumptions of both models. In order to estimate the acoustically driven flows analytically, Lighthills approach is based on some fundamental simplifications that are not necessary for

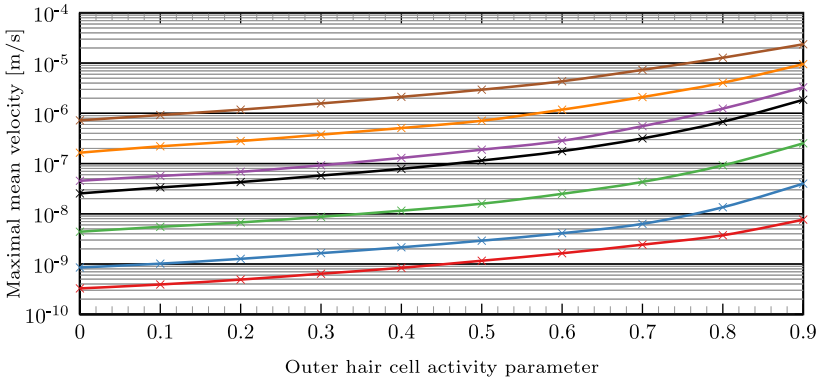

(a)

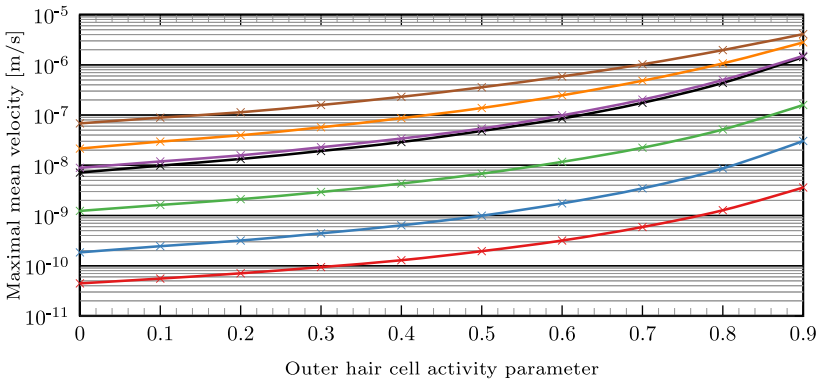

(b)

Fig. 14. (Color online) (a) shows the Eulerian specification of the maximal mean velocity outside the Stokes boundary layer that are determined by the computational model. By comparison, (b) illustrates Lighthill's estimate[2] of the maximal mean velocity. The velocities are calculated on the basis of the numerical results of the first-order system at different frequencies and outer hair cell activities: 128 (red line), 256 (blue line), 512 (green line), 1024 (black line), 2048 (purple line), 4096 (orange line) and 8192 Hz (brown line).

the numerical approach presented here. Nevertheless, another reason for the deviations can also be found in numerical errors, especially due to the very small dimensions of the Stokes boundary layer.

4.2.2. *Békésy's eddies*

The numerical simulation of the computational model has shown that acoustic streaming is mainly driven by boundary layer mechanisms (cf. Chap. 4.2.1). Acoustically driven flows that are based on mass-transport mechanisms are not as significant as the previously mentioned phenomenon. As shown in Fig. 15, the mean fluid motion of second-order can be best described by two eddies, which are almost symmetrically arranged to the cochlear partition. Of course, this circular movement must be thought of as superimposed by the first-order fluctuations. But a separated evaluation is useful, since both motions can be described on

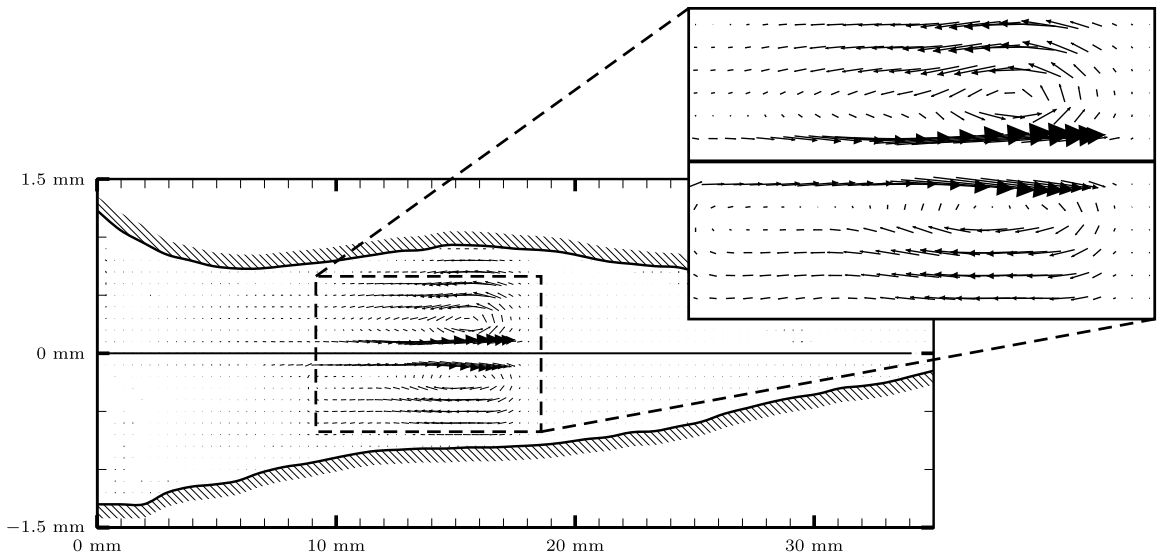

(a)

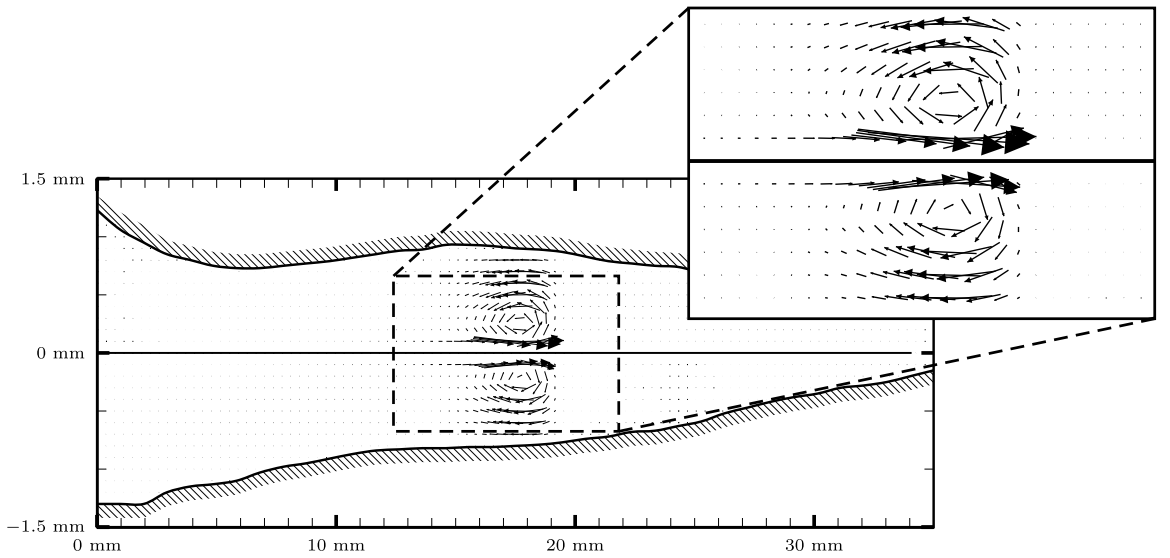

(b)

Fig. 15. The Lagrangian mean velocity field of the second-order system at a stimulation frequency of 1024 Hz in the passive (a) and the active (b) cochlea model. The flow field constitutes a first-order approximation of acoustic streaming and is characterized by two eddies above and below the cochlear partition near to the characteristic place.

different time-lines due to their difference between both velocities. The direction of the rotation of each eddy is specified by a movement toward the apex for fluid particles that are located directly next to the partition. Thus, an opposite directed flow occurs close to the outer boundary. The velocity of each eddy varies along its streamlines. Next to the cochlear

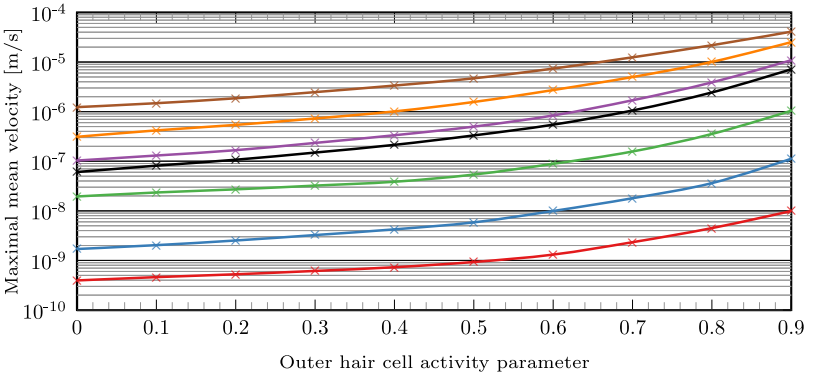

Fig. 16. (Color online) Lagrangian specification of the maximal mean velocity at different stimulation frequencies and outer hair cell activities: 128 (red line), 256 (blue line), 512 (green line), 1024 (black line), 2048 (purple line), 4096 (orange line) and 8192 Hz (brown line).

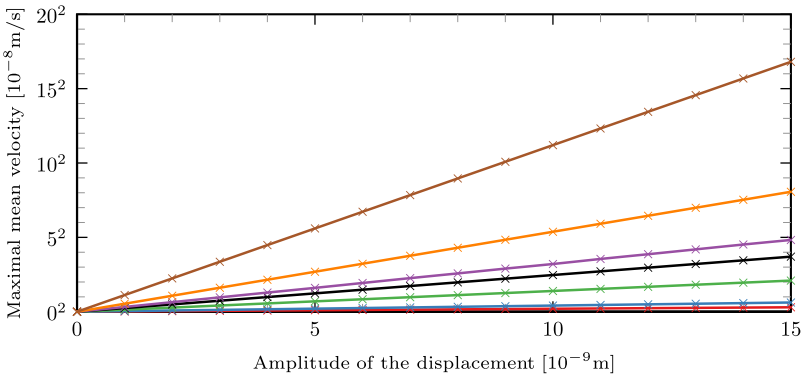

(a)

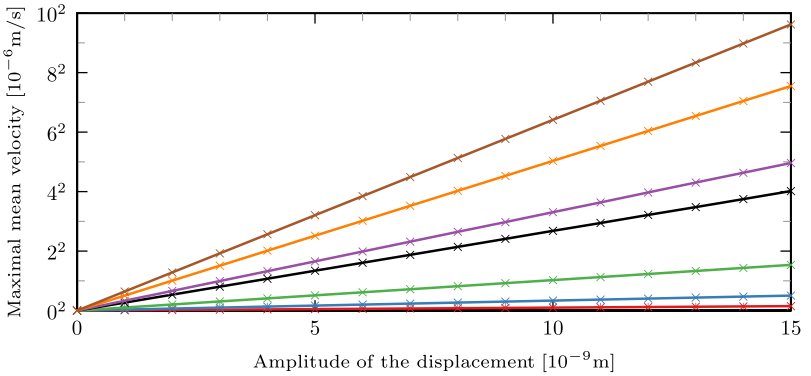

(b)

Fig. 17. (Color online) Maximal mean velocity (Lagrangian specification) at different stimulation frequencies and stimulation amplitudes in the passive cochlea model (a) as well as in the active model (b) 128 (red line), 256 (blue line), 512 (green line), 1024 (black line), 2048 (purple line), 4096 (orange line) and 8192 Hz (brown line).

partition, the fluid is accelerated until a point of maximal velocity is reached. Shortly behind the position of maximal velocity, the direction of the fluid motion turns back and the velocity decreases. The maximal mean velocities at different stimulation frequencies, stimulation amplitudes and outer hair cell activity parameters are illustrated in Figs. 16 and 17.

Dependency of the frequency: The longitudinal position of the center of each eddy is nearly identical to the position of the maximal displacement of the basilar membrane.

Dependency of the amplitude: As it can be seen in Fig. 17, the maximal velocity of the mean flow is proportional to the square of the stimulation amplitude. Such a quadratic dependence on the velocity was also observed by the experiments from Tonndorf.[4] In addition, the results indicate that the amplitude has no (significant) influence on the shape of the eddies. In other words, the change of the amplitude causes only a spatially uniform (scalar) scaling of the vector field that represents the mean flow.

Dependency of the outer hair cell amplification: Figure 16 illustrates that the velocity of the acoustically driven flows grows almost exponentially with the outer hair cell activity parameter. But in contrast to the amplitude, this growth depends on various factors such as the gain of the displacement of the basilar membrane, the phase velocity of the traveling wave and its envelope. Furthermore, the activity parameter also influences the shape of the eddies. By comparing the eddies of the active model with the passive model (cf. Chap. 15) it can be clearly seen that the outer hair cell driven amplification process is accompanied with a decrease of the eddy size.

In summary, it can be noted that the numerical results are almost in conformity with the experimental studies from Tonndorf.[4]

5. Conclusion

This work was concerned with the numerical simulation of acoustically driven flows within the inner ear. It is the first time that the occurrence and magnitude of acoustic streaming was successfully analyzed on the basis of a computational model. The relevance of acoustic streaming with respect to its physiological impact on the mechanisms of hearing is still an open question. Therefore, the results of this work provide instruments in order to support the discussion about the influence of nonlinear flow effects within the cochlea.

Up to now, acoustically driven flows were either examined by performing experiments on mechanical models[4] or on the basis of analytical considerations.[1,2] As mentioned by Tonndorf,[4] mechanical models have the advantage of allowing direct observation of nonlinear mean flows. But due to a different scaling of the mechanical model in relation to the human cochlea, the experiments can only provide information about the principle structure of a potential mean flow. Furthermore, the mechanical model has some significant limitations concerning its usability, for example with respect to the stimulation amplitude and the frequency range.

In contrast, Lighthill[2] analytically derived an estimate of the magnitude of acoustic streaming outside the Stokes boundary layer near to the characteristic place. But his analytical model is based on substantial simplifications and it does not describe the concrete flow field of the secondary mean motion.

The computational model presented in this work overcomes most of these difficulties. On the one hand the model has been performed on the basis of realistic dimensions with regard to the physical properties and, furthermore, there has been no constraints concerning the usability as in the case of mechanical model. On the other hand, the simplifications made by the modeling process are not as substantial as in an analytical model. In this context it should be emphasized that the computational model provides information about both the structure of the secondary flow field as well as the magnitude of the mean motion.

In comparison to other cochlea models, a very comprehensive and complex model has been developed in order to be able to simulate the acoustically driven flows within the inner ear. The complexity of the presented model is the result of the explicit consideration of the dynamical behavior of three major components: the fluid, the basilar membrane and the outer hair cell motility.

Particular attention has been paid to an appropriate representation of the fluid in order to ensure that the system yields accurate results with respect to the linear and nonlinear flow motions. The dynamics of the fluid were simulated by using concepts from the field of continuum mechanics.

The consideration of the interactions of the fluid with the biological structure that separates the scala tympani from the scala vestibular was a very important aspect in order to virtually reproduce the characteristic flow field. Therefore, the cochlear partition was modeled as an oscillatory system as suggested by Mammano and Nobili.[19] But in contrast to the model from Mammano and Nobili, the external hydrodynamic forces have been directly calculated on the basis of the fluid dynamics and not with the help of a phenomenological approach. While the dynamical reaction of the basilar membrane was evaluated in the time domain, Mammano and Nobili examined the displacements of the cochlear partition in the frequency domain.

The displacement pattern of the basilar membrane and also the flow field of the fluid significantly differ between the active case, where the outer hair cell motility is taken into account, and the passive case, where this amplification mechanism is neglected. Therefore, the effect of the outer hair cell motility on the resultant secondary flow field has also been analyzed. The additional force exerted by the outer hair cells was calculated on the basis of an approach suggested by Mammano and Nobili,[19,20] who modeled the amplification mechanisms as an additional oscillatory subsystem.

In summary, a set of different differential equations and boundary conditions were deduced that describe the complex dynamics of the whole cochlear system. By the use of a well-known approach from the perturbation theory, it was possible to split the system of equations into a set of successive linear subsystems. With regard to the numerical simulation of acoustic streaming, this perturbation approach was so far only used in the context

of pure fluidic systems. Therefore, it is the first time that this approach was extended to an highly fluid-structure coupled problem like the cochlea.

The resultant first-order subsystem describes the linear acoustic reaction of the system. The spatial discretization of this acoustic system, performed by means of the finite element method, resulted in a system of ordinary differential equations, which, in turn, was discretized by using an implicit integration method. Due to the strong coupling between the fluid, the basilar membrane and the outer hair cell motility, the different processes were synchronously solved by a monolithic approach. The simulation of this linear acoustic reaction was a very computationally intensive part of the whole process, but the accurate calculation of the first-order solution was a crucial requirement for the successful determination of the second-order mean flows.

The results of this first-order subsystem were compared to the results of other experimental studies and analytical considerations. It has been shown that an harmonic stimulation at the oval window induces the expected typical traveling wave motion of the cochlear partition. Furthermore, the relationship between the stimulation frequency and the associated characteristic places complies with empirical experiments.[25] It has been proven that the main cause for acoustically driven flows can be found in a boundary layer driven mechanism. Therefore, particular attention has been paid to the fluid motions within the thin Stokes boundary layer of the cochlear partition, which comply, in the main, with analytical approximations developed by Lighthill[2] on the basis of theoretical considerations from Lord Rayleigh.[36]

If the outer hair cell motility is taken into account by the simulation process, the traveling wave pattern will, inter alia, be locally enhanced near to the characteristic place. This significant amplification is, in addition, accompanied with an increased phase lag and an apical peak shift as also observed by Mammano and Nobili[19] in their computational model. It should be noted that the linearized model of the outer hair cell motility cannot be used to reproduce the nonlinear behavior of the amplification mechanism. Nevertheless, it has been shown that this linear model was an appropriate instrument to analyze the effect of the outer hair cell driven amplification on the resultant mean flows.

The time-averaged second-order subsystem yielded a first-order approximation of the acoustically driven flows within the inner ear. The application of the finite element method resulted in a stationary system of equations where the right-hand vector includes the results of the first-order system in terms of a virtual force- and mass-source distributions.

The resultant acoustic streaming flow field is in accordance with the experimental studies from Tonndorf.[4] Furthermore, the results of the numerical simulations indicate that the maximal velocity of the acoustically driven flows is up to one order of magnitude larger than the analytical estimates from Lighthill.[2]

6. Outlook

This paper opens up a variety of new opportunities for further research activities. The numerical estimations of acoustic streaming presented in this paper allow a more

substantiated discussion of the mean flows on the physiological impact in hearing. Also the model itself shows some potential for further improvements. For example, an extension for a full three-dimensional examination would be desirable. Furthermore, the numerical approach should be further investigated in terms of accuracy, convergence and grid dependency.

References

1. W. L. Hallauer, Nonlinear mechanical behavior of the cochlea, Ph.D thesis, Stanford University, (1974).
2. M. J. Lighthill, Acoustic streaming in the ear itself, *J. Fluid Mech.* **239**(1) (1992) 551–606.
3. G. Von Békésy, Experiments in hearing (1960).
4. J. Tonndorf, Nonlinearities in cochlear hydrodynamics, *J. Acoust. Soc. Am.* **47** (1970) 579.
5. S. Boluriaan and P. J. Morris, Acoustic streaming: From rayleigh to today, *Int. J. Aeroacoust.* **2**(3) (2003) 255–292.
6. D. Köster, Numerical simulation of acoustic streaming on surface acoustic wave-driven biochips, *SIAM J. Sci. Comput.* **29** (2007) 2352.
7. C. E. Bradley, Acoustic streaming field structure: The influence of the radiator, *J. Acoust. Soc. Am.* **100** (1996) 1399.
8. E. Givelberg and J. Bunn, A comprehensive three-dimensional model of the cochlea* 1, *J. Comput. Phys.* **191**(2) (2003) 377–391.
9. L. Cheng, R. D. White and K. Grosh, Three-dimensional viscous finite element formulation for acoustic fluid-structure interaction, *Comput. Methods Appl. Mech. Eng.* **197**(49–50) (2008) 4160–4172.
10. F. Böhnke and W. Arnold, 3d-finite element model of the human cochlea including fluid-structure couplings, *ORL J. Otorhinolaryngol. Relat. Spec.* **61**(5) (1999) 305–310.
11. K. M. Lim and C. R. Steele, A three-dimensional nonlinear active cochlear model analyzed by the wkb-numeric method, *Hear. Res.* **170**(1) (2002) 190–205.
12. Y. J. Yoon, C. R. Steele and S. Puria, Feed-forward and feed-backward amplification model from cochlear cytoarchitecture: An interspecies comparison, *Biophys. J.* **100**(1) (2011) 1–10.
13. J. Wysocki, Dimensions of the human vestibular and tympanic scalae, *Hear. Res.* **135**(1–2) (1999) 39–46.
14. J. N. Reddy and D. K. Gartling, *The Finite Element Method in Heat Transfer and Fluid Dynamics*, 3rd edn. (CRC Press, 2010).
15. R. Greve, *Kontinuumsmechanik* (Springer, 2003).
16. J. H. Spurk and N. Aksel, *Fluid Mechanics* (Springer, 2007).
17. M. J. Lighthill, Acoustic streaming, *J. Sound Vib.* **61**(3) (1978) 391–418.
18. M. van Dyke, *Perturbation Methods in Fluid Mechanics* (Parabolic Press, 1975).
19. F. Mammano and R. Nobili, Biophysics of the cochlea: Linear approximation, *J. Acoust. Soc. Am.* **93** (1993) 3320.
20. R. Nobili, A. Vetešnik, L. Turicchia and F. Mammano, Otoacoustic emissions from residual oscillations of the cochlear basilar membrane in a human ear model, *J. Assoc. Res. Otolaryngol.* **4**(4) (2003) 478–494.
21. J. Ashmore, Cochlear outer hair cell motility, *Physiol. Rev.* **88**(1) (2008) 173.
22. L. Robles and M. A. Ruggero, Mechanics of the mammalian cochlea, *Physiol. Rev.* **81**(3) (2001) 1305.
23. E. S. Olson, Direct measurement of intra-cochlear pressure waves, *Nature* **402**(6761) (1999) 526–529.

24. E. S. Olson, Harmonic distortion in intracochlear pressure and its analysis to explore the cochlear amplifier, *J. Acoust. Soc. Am.* **115** (2004) 1230.
25. D. D. Greenwood, A cochlear frequency-position function for several species—29 years later, *J. Acoust. Soc. Am.* **87** (1990) 2592.
26. Christiane Förster, *Robust Methods for Fluid-structure Interaction with Stabilised Finite Elements* (Stuttgart, 2007).
27. J. C. Houbolt, A recurrence matrix solution for the dynamic response of elastic aircraft, *J. Aeronaut. Sci.* **17** (1950) 540–550.
28. Klaus-Jürgen Bathe and P. Zimmermann, *Finite-Elemente-Methoden* (Springer, 2001).
29. Y. Saad and M. H. Schultz, Gmres: A generalized minimal residual algorithm for solving nonsymmetric linear systems, *SIAM J. Sci. comput.* **7**(3) (1986) 856–869.
30. Y. Saad, *Iterative Methods for Sparse Linear Systems* (PWS Publishers, 1996).
31. P. Dallos, The active cochlea, *J. Neurosci.* **12**(12) (1992) 4575.
32. P. M. Sellick, R. Patuzzi and B. M. Johnstone, Measurement of basilar membrane motion in the guinea pig using the Mossbauer technique, *J. Acoust. Soc. Am.* **72** (1982) 131.
33. P. M. Sellick, G. K. Yates and R. Patuzzi, The influence of Mossbauer source size and position on phase and amplitude measurements of the guinea pig basilar membrane, *Hear. Res.* **10**(1) (1983) 101–108.
34. B. M. Johnstone, R. Patuzzi and G. K. Yates, Basilar membrane measurements and the travelling wave, *Hear. Res.* **22**(1–3) (1986) 147–153.
35. A. L. Nuttall and D. F. Dolan, Steady-state sinusoidal velocity responses of the basilar membrane in guinea pig, *J. Acoust. Soc. Am.* **99** (1996) 1556.
36. L. Rayleigh, *Theory of Sound*, Vol. 2 (Macmillan, 1896).